Competition between Förster Resonance Energy Transfer and Electron Transfer in Stoichiometrically Assembled Semiconductor Quantum Dot–Fullerene Conjugates

Michael H. Stewart,[†,△,*] Alan L. Huston,[†,△] Amy M. Scott,[§] Eunkeu Oh,[†,∥] W. Russ Algar,[‡,⊥] Jeffrey R. Deschamps,[‡] Kimihiro Susumu,[†,∥] Vaibhav Jain,[†] Duane E. Prasuhn,[‡] Juan Blanco-Canosa,[#] Philip E. Dawson,[#] and Igor L. Medintz[‡,*]

[†]Optical Sciences Division, Code 5611, [‡]Center for Bio/Molecular Science and Engineering, Code 6900, U.S. Naval Research Laboratory, Washington, DC 20375, United States, [§]Department of Chemistry, Columbia University, New York, New York 10027, United States, [⊥]Department of Chemistry, University of British Columbia, Vancouver, BC V6T 1Z1, Canada, [∥]Sotera Defense Solutions, Annapolis Junction, Maryland 20701, United States, and [#]Departments of Cell Biology and Chemistry, The Scripps Research Institute La Jolla, California 92037, United States. [△]M.H.S. and A.L.H. contributed equally.

ABSTRACT Understanding how semiconductor quantum dots (QDs) engage in photoinduced energy transfer with carbon allotropes is necessary for enhanced performance in solar cells and other optoelectronic devices along with the potential to create new types of (bio)sensors. Here, we systematically investigate energy transfer interactions between C_{60} fullerenes and four different QDs, composed of CdSe/ZnS (type I) and CdSe/CdS/ZnS (quasi type II), with emission maxima ranging from 530 to 630 nm. C_{60}-pyrrolidine tris-acid was first coupled to the N-terminus of a hexahistidine-terminated peptide *via* carbodiimide chemistry to yield a C_{60}-labeled peptide ($pepC_{60}$). This peptide provided the critical means to achieve ratiometric self-assembly of the QD-($pepC_{60}$) nanoheterostructures by exploiting metal affinity coordination to the QD surface. Controlled QD-$(pepC_{60})_N$ bioconjugates were prepared by discretely increasing the ratio (N) of $pepC_{60}$ assembled per QD in mixtures of dimethyl sulfoxide and buffer; this mixed organic/aqueous approach helped alleviate issues of C_{60} solubility. An extensive set of control experiments were initially performed to verify the specific and ratiometric nature of QD-$(pepC_{60})_N$ assembly. Photoinitiated energy transfer in these hybrid organic–inorganic systems was then interrogated using steady-state and time-resolved fluorescence along with ultrafast transient absorption spectroscopy. Coordination of $pepC_{60}$ to the QD results in QD PL quenching that directly tracks with the number of peptides displayed around the QD. A detailed photophysical analysis suggests a competition between electron transfer and Förster resonance energy transfer from the QD to the C_{60} that is dependent upon a complex interplay of $pepC_{60}$ ratio per QD, the presence of underlying spectral overlap, and contributions from QD size. These results highlight several important factors that must be considered when designing QD-donor/C_{60}-acceptor systems for potential optoelectronic and biosensing applications.

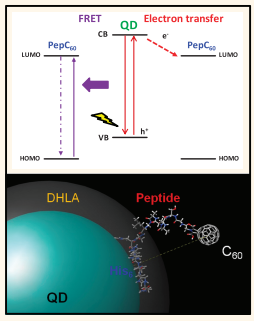

KEYWORDS: Semiconductor · quantum dot · peptide · fullerene · electron transfer · C_{60} · FRET · dipole · resonance · carbon allotrope · metal affinity · coordination · spectral overlap

Semiconductor quantum dots (QDs) are being actively integrated into optoelectronic devices such as solar cells, light emitting diodes, and photodetectors along with a variety of biosensing and bioimaging assemblies where they hold much promise for improving the performance of those technologies.[1−9] In order to optimize their utility in these and other applications, it is important to understand charge and energy transfer at the QD interface.[9] Knowledge of these processes within the context of QD-bioconjugates in particular has been harnessed to create sophisticated biosensors where signal modality is based on changes in the degree of Förster resonance energy transfer (FRET) or charge transfer (CT) between QDs and proximal donors or acceptors.[10,11] For example, Algar et al. recently demonstrated the first application of QDs as simultaneous donors and acceptors in a time-gated FRET relay for the multiplexed

* Address correspondence to Michael.stewart@nrl.navy.mil, Igor.medintz@nrl.navy.mil.

Received for review July 25, 2013 and accepted September 25, 2013.

Published online October 15, 2013
10.1021/nn403872x

detection of protease activity based on a single color of QD (one emission wavelength).[12] In contrast to the current state-of-the-art, multiplexing was achieved with a single QD emitter rather than utilizing multiple QDs, where each would be required to have a different and spectrally resolved emission wavelength. To achieve similar success in improving the efficiency of QD-based optoelectronic and other biosensing devices, a more detailed understanding of energy/CT interactions between QDs and a wide array of electronically relevant donor/acceptor materials is required.[1−9]

Although a variety of fluorescent and electroactive materials are currently under investigation for pairing with QDs, interactions with carbon allotropes including buckminsterfullerene (C_{60}), carbon nanotubes, and carbon nanocups are of particular interest as they have been proposed to enhance photoinduced electron transfer (ET) in solar cell constructs while also suggesting strong potential for new types of biosensing and biodelivery formats.[13−21] The design principle behind these donor−acceptor systems is to combine the outstanding light absorption efficiency of QDs with the exceptional ET acceptor capacity of carbon allotropes. In particular, QD−C_{60} conjugates are being intensely investigated for their potential use as core charge-separation units in solution-processable optoelectronic devices. In order to achieve homogeneous, solution phase self-assembly of QD−fullerene conjugates, one must take advantage of the well-known surface chemistry of QDs and overcome challenges with the very low intrinsic solubility of C_{60}. Several strategies have been used to prepare homogeneous assemblies of QDs and C_{60} derivatives in order to study their photophysical interactions. Guldi et al. demonstrated electrostatic self-assembly of cationic C_{60} derivatives and anionic CdTe QDs in aqueous solutions resulting in QD quenching and a long-lived fullerene radical anion which was detected in the near-infrared (NIR).[22] While this process achieved an association constant of $\sim 10^5\ M^{-1}$, electrostatic assembly does not always provide for precise control over stoichiometry and long-term stability and can be limited by susceptibility to dissociation under certain conditions. Complementary hydrogen bonding interactions have also been used to assemble QD−C_{60} constructs.[23] Ideally, the association between QD and C_{60} should be more robust, such as that obtained through covalent linkages or coordination interactions. Fullerenes displaying functional groups such as thiols[13,24] and carboxyls[14,25] have an affinity for some QD surfaces, and this affinity has been used to facilitate the self-assembly of QD−fullerene conjugates in solution. Bang and Kamat utilized thiolated-C_{60} to prepare CdSe QD−C_{60} nanocomposites where the ET rate constant increased with decreasing size of the CdSe QD and was far higher than equivalent amounts of materials that were simply mixed together.[13] Song et al. prepared QD−C_{60} complexes with a carboxyl-functionalized fullerene and performed detailed spectroscopic analysis of ensemble and single-QD measurements to elucidate ET dynamics in the system.[14] These and other studies have provided an initial working description of the photophysical interactions between QDs and fullerenes and have primarily identified ET as the predominant pathway for deactivation of the QD excited state.

While it is generally accepted that excited state QDs are deactivated (quenched) by fullerenes *via* photoexcited CT, the possibility of a FRET interaction should not be overlooked due to the spectral overlap between visible-emitting CdSe-based QDs and C_{60} (*vide infra*). Indeed, numerous reports suggest that QD donor−acceptor interactions with other carbon allotropes such as graphene, graphene oxide, and carbon nanotubes may involve CT, FRET, or both.[26−32] Thus, an analysis of the photophysical interactions in hybrid QD−C_{60} nanostructures accounting for the possibility of FRET in addition to ET is still warranted, and improved methods for assembling these composites would certainly benefit this endeavor. Ideally, the chemistry utilized to assemble the QD−C_{60} hybrids should be (i) facile to implement; (ii) repeatable; (iii) provide for control over the ratio or valence of C_{60} assembled per QD; (iv) robust and high affinity; and (v) applicable to multiple different QD preparations (vi) and allow for control over the QD−C_{60} separation distance such that the C_{60} was not in direct contact with the QD surface to prevent contact-based quenching. Hexahistidine- (His_6) driven metal affinity coordination of proteins, peptides, and even appropriately modified DNA to ZnS coated QD surfaces has been extensively used to assemble a variety of QD bioconjugates for sensing and cellular delivery applications.[33−35] This methodology provides several advantages over previous techniques used to assemble and study QD−C_{60} hybrids, including (i) rapid assembly of well-defined conjugates in a facile and high affinity manner, (ii) exceptional control over the ratio of C_{60} per QD, and (iii) control of their separation distance.[36]

Here, we investigate energy transfer interactions between C_{60} and QDs (composed of CdSe/ZnS and CdSe/CdS/ZnS) tethered by a peptide bridge (see schematic in Figure 1). First, C_{60}-pyrrolidine tris-acid was coupled to the N-terminus of a His_6-terminated peptide using carbodiimide chemistry to yield a C_{60}-labeled peptide (pepC_{60}). The peptide provided a means to achieve ratiometric self-assembly of the QD−pepC_{60} nanoheterostructures *via* metal affinity coordination. We show that metal affinity coordination of peptides to QD surfaces, which has always been carried out in aqueous solutions, is also effective in aqueous mixtures of dimethyl sulfoxide (DMSO) and provides ratiometrically controlled QD−pepC_{60} bioconjugates; this approach helps alleviate issues of C_{60} solubility. Assemblies were prepared with

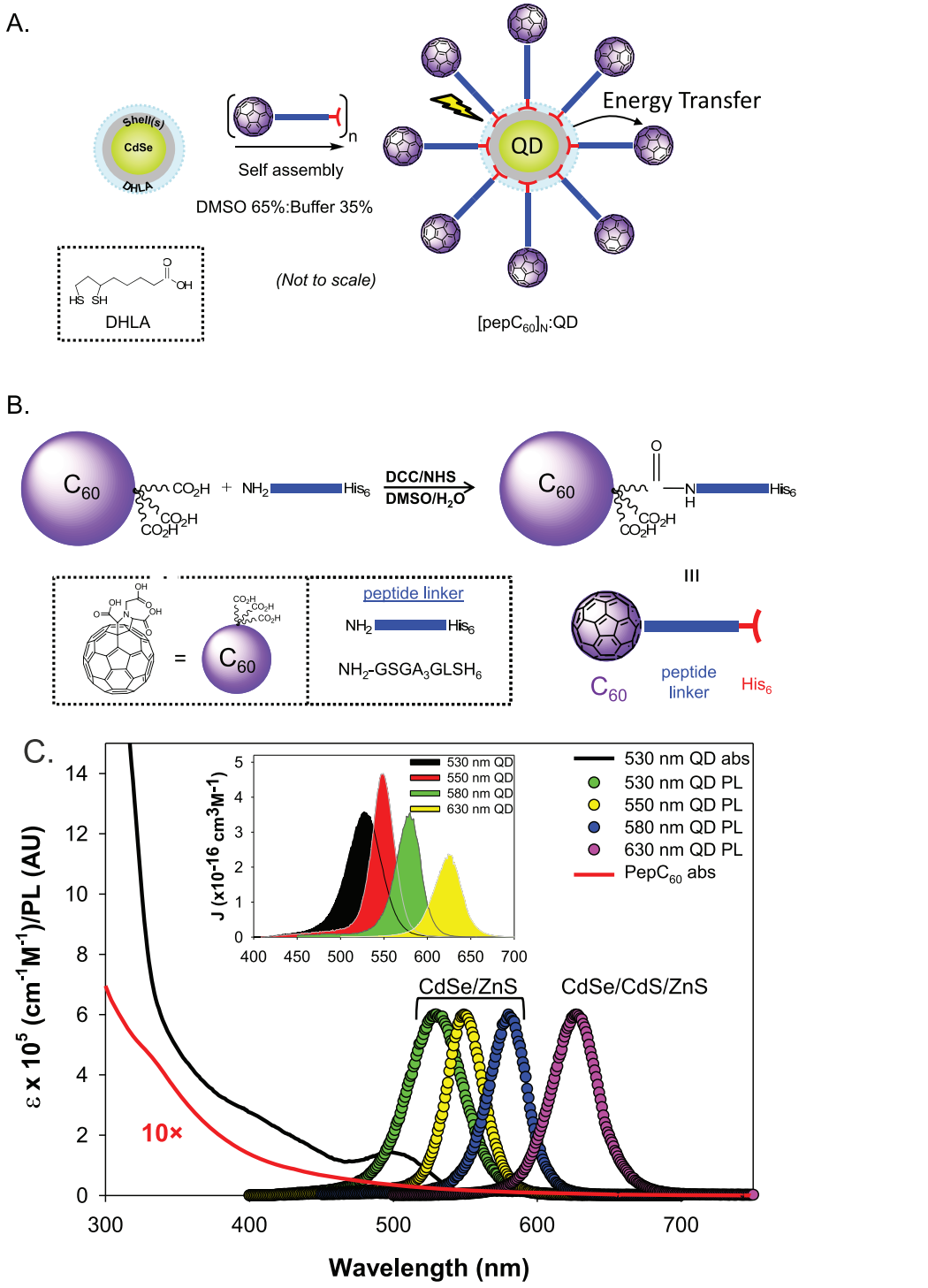

Figure 1. Synthesis of pepC$_{60}$ and self-assembly to DHLA-coated QDs. (A) The C$_{60}$-modified peptide is ratiometrically self-assembled to the surface of DHLA-coated QDs driven by the metal affinity coordination of the (His)$_6$-sequence. (B) C$_{60}$-pyrrolidine tris-acid is covalently coupled to the unique primary amine on the peptide linker *via* carbodiimide chemistry. (C) Selected absorption and emission spectra of the four DHLA-coated QDs and the pepC$_{60}$. The pepC$_{60}$ absorbance plot is displayed at a 10× value to highlight overlap. Inset shows the spectral overlap function for each of the putative QD donors with the pepC$_{60}$ acceptor. Note the consistent decrease in spectral overlap with increasing wavelength.

increasing ratios of pepC$_{60}$ per QD, and photoinitiated energy transfer in these systems was interrogated by both steady-state and time-resolved fluorescence along with femtosecond transient absorption (fsTA) studies. Coordination of pepC$_{60}$ to the QDs results in QD PL quenching that tracks with the number of peptides per QD. A detailed photophysical analysis suggests a competition between ET and FRET with a strong dependence on the degree of donor–acceptor spectral overlap.

TABLE 1. Relevant QD and QD-C_{60} FRET and Photophysical Properties

QD	530 nm QD	550 nm QD	580 nm QD	630 nm QD
core/shell composition	CdSe/ZnS	CdSe/ZnS	CdSe/ZnS	CdSe/CdS_{3ML}/$ZnS_{3.5ML}$[a]
Type	I	I	I	quasi type II
QY	0.23	0.14	0.14	0.13
core diameter (nm)[b]	2.4	2.5	3.3	3.7
final TEM size (nm)[b]	3.0 ± 0.4	4.5 ± 0.7	4.8 ± 0.8	7.7 ± 0.5
ZnS shell thickness (nm)	0.30	1	0.75	~1.0
QD extinction coefficient (M^{-1} cm^{-1})[c]	118 000 (498 nm)	158 000 (531 nm)	326 000 (564 nm)	301 000 (594 nm)
$pepC_{60}$ extinction coefficient (M^{-1} cm^{-1})[d]	2,340	1,810	1,150	590
overlap integral $J \times 10^{-14}$ (cm^3 M^{-1})	1.88	1.68	1.38	0.96
Förster distance R_0 (Å)	29.8	26.9	26.0	24.2
predicted separation distance r (Å)[e]	56	63	65	79

[a] ML = estimated monolayers present based on the synthetic conditions used. [b] Representative TEM data in the SI. [c] Corresponding to the first exciton absorption band as indicated by the wavelength in parentheses. [d] $PepC_{60}$ extinction coefficient at QD PL maxima, values shown for ratios of 1-C_{60} per QD. [e] Assumes at least ±10 Å freedom of movement.

RESULTS

QDs and Peptide-Modified C_{60} Preparation. As shown in Figure 1A, the functional architecture underpinning this study is a central QD surrounded by multiple C_{60} molecules attached through self-assembled peptide bridges. Two different types of QDs were prepared for this study, (i) prototypical type I CdSe/ZnS core/shell and (ii) quasi type II CdSe/CdS/ZnS core/shell/shell QDs. The CdSe/ZnS QDs were synthesized by starting with three sizes of the CdSe core which were then overcoated with a wider-band gap ZnS shell to yield QDs with emission maxima centered at ~530, 550, and 580 nm. In these structures the exciton is expected to remain predominantly confined to the CdSe core. The 630 nm CdSe/CdS/ZnS QDs contain three components that include a quasi type II CdSe/CdS core/shell interior surrounded by a wider-band gap ZnS shell. The quasi type II CdSe/CdS arrangement should allow photoexcited electrons to leak into the CdS layer[37] while the final ZnS shell passivates surface defects for higher quantum yields and still provides a surface for assembling the His_6-terminated $pepC_{60}$. It was important to have a ZnS shell on all four QDs so that the peptide would have uniform affinity for all QD surfaces. QDs were transferred to water following cap exchange with DHLA as described in the Methods. The compact DHLA coating should allow for a relatively close proximity between the $pepC_{60}$ moiety and the QD surface, optimizing for the highly distance-dependent nature of energy transfer interactions. Furthermore, the negatively charged DHLA coating potentially provides some electrostatic repulsion between the QD and the remaining carboxyl groups on the C_{60} moiety to preclude contact-based quenching between the two. Physical and photophysical properties of the QDs are summarized in Table 1, and selected absorption and emission spectra of QDs and the $pepC_{60}$ are shown in Figure 1C. The inset shows the corresponding spectral overlap functions between the $pepC_{60}$ and the QDs and reveals that non-negligible spectral overlap exists between the four Gaussian-shaped QD emission profiles and the $pepC_{60}$ absorption spectrum. The corresponding overlap integral values (J) are in the range (0.96−1.88) × 10^{-14} cm^3 M^{-1}, which translate to Förster distances (R_0) between 29.8 and 24.2 Å for the 530−630 nm QD samples, respectively (Table 1).

The carboxyl groups of C_{60}-pyrrolidine tris-acid used in this study provide the C_{60} with a very modest degree of water solubility as well as a chemical handle for conjugating the C_{60} to a 15-mer peptide GS•GAAAG•LS•HHHHHH (Figure 1B). This modular peptide (designated by the breaks in the sequence) was recently used to prepare assemblies of QDs with a weakly phosphorescent redox-active osmium polypyridyl complex and serves a similar purpose here.[38] Carbodiimide chemistry was used to covalently couple one of the carboxyl groups on the C_{60}-pyrrolidine tris-acid to the unique N-terminal amine group of the first glycine residue. The GAAAG sequence serves as a spacer where a partial Ala-helix is bordered by two glycine residues. The leucine-serine sequence provides rotational freedom to the C-terminal His_6 sequence, which facilitates metal affinity coordination of the peptide to the QD surface. The imidazole groups in the His-tag coordinate to the zinc on the QD surface with high affinity and stability (K_d^{-1} ~10^9 M^{-1}).[39] This self-assembly process typically allows for facile and exceptional control over the number of C_{60} moieties per QD upon mixing in buffer (Figure 1A).[36,40]

Ratiometric Metal Affinity Coordination of $PepC_{60}$ to QDs. Typically, the His-tag self-assembly of peptides to QDs is performed in buffered aqueous solutions. Due to the hydrophobic nature of C_{60} and the fact that one of its three solubility-promoting carboxyl groups is coupled to a peptide, we utilized a DMSO/buffer mixture to ensure complete dissolution of the $pepC_{60}$, avoiding complications from aggregation in neat buffer. Therefore, we started with a series of control experiments to confirm that self-assembly between the His_6-peptide and the zinc-rich QD surface was still efficient under these conditions. Full confidence in the specificity and

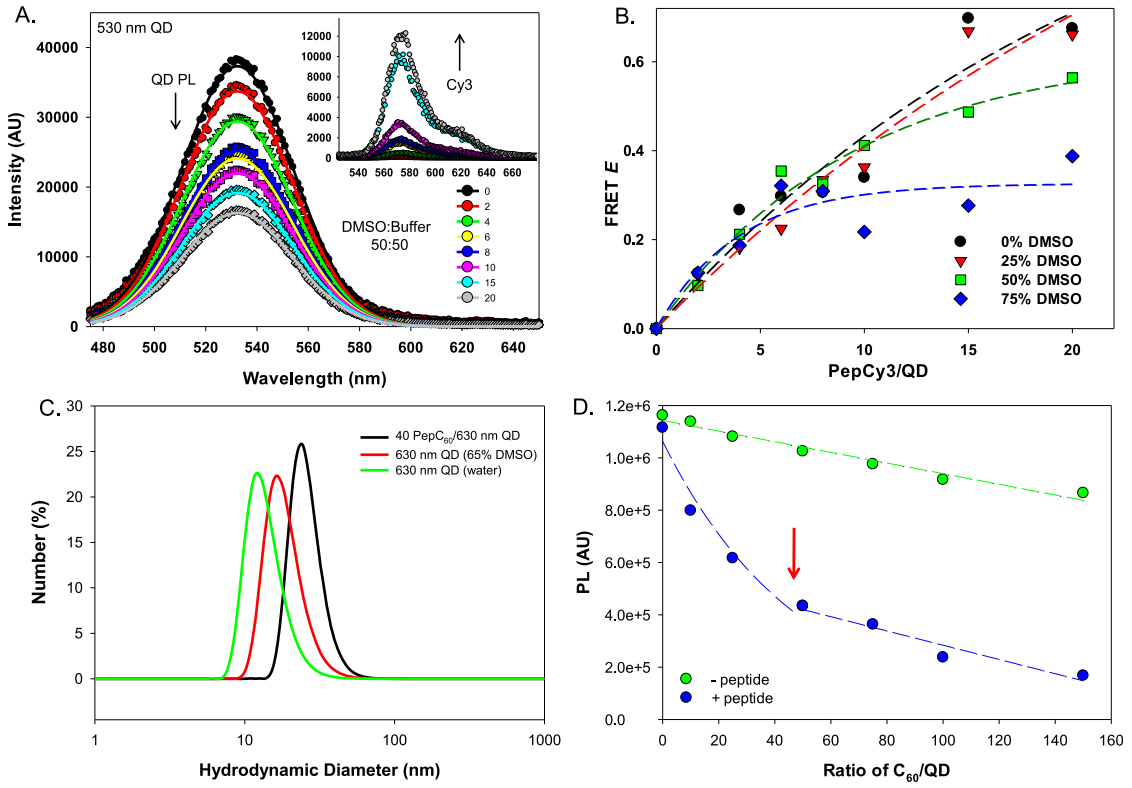

Figure 2. Control experiments to verify peptide self-assembly to QDs in DMSO/buffer mixtures. (A) FRET assay. Deconvolved 530 nm QD quenching data and sensitized Cy3 emission (inset) from increasing ratios of pepCy3 self-assembled to QDs in 50% DMSO/tetraborate buffer pH 8.5. The Cy3/QD ratios are indicated under the inset. Data from experiments with 0%, 25%, and 75% DMSO/buffer solutions are found in SI Figure S1. Individual solutions of DMSO and buffer were mixed together and then the corresponding amounts of QD and pepCy3 added and allowed to self-assemble prior to collection of fluorescence. Samples were excited at 300 nm. (B) Plot of FRET *E versus* Cy3-labeled acceptor peptide collected with increasing concentrations of DMSO in the buffer. (C) Dynamic light scattering assay. Plot of number profile (%) versus hydrodynamic diameter (D_H in nm) for (i) 630 nm emitting QDs in water, (ii) 630 nm QDs in 65% DMSO, (iii) and 630 nm QDs assembled with 40 pepC_{60} in 65% DMSO. Note the increase in D_H with peptide assembly. (D) Peptide mediated quenching test. PL quenching data for 550 nm QDs treated with increasing ratios of C_{60}-pyrrolidine tris-acid (− peptide) and pepC_{60} (+ peptide) in 75% DMSO/buffer. Note the bimodal curve obtained from the + peptide sample as highlighted by the red arrow. Samples were excited at 300 nm.

ratiometric nature of this assembly was critical for the subsequent data analysis.

First, a FRET efficiency assay was performed where a His_6-peptide N-terminally labeled with Cy3 (pepCy3) was self-assembled to 530 nm QDs in neat borate buffer (0% DMSO), 1:3 DMSO/borate buffer (25% DMSO), 1:1 DMSO/borate buffer (50% DMSO), and 3:1 DMSO/borate buffer (75% DMSO). Samples were assembled and collected as described in the Materials and Methods. Figure 2A shows the deconvoluted steady-state PL spectra of 530 nm QDs self-assembled with increasing amounts of pepCy3 in 50% DMSO (ratios of 0−20 pepCy3/QD). The inset of Figure 2A shows the FRET-sensitized pepCy3 emission, which has been corrected for the direct excitation of pepCy3. Raw steady-state PL data for the QDs in 0%, 25%, and 75% DMSO are also shown in the Supporting Information (SI) Figure S1. Figure 2B plots the observed FRET efficiency (*E*) versus Cy3-labeled acceptor peptide collected with increasing concentrations of DMSO in the buffer. In 50% DMSO, the magnitude of QD PL quenching increases with the ratio of pepCy3/QD, where ~43% QD PL is retained at *ca.* 20 pepCy3/QD. The average difference in FRET *E* between 0% DMSO and 50% DMSO over all ratios tested was only 3.6%. The major deviation in apparent FRET *E* appears for the 75% DMSO solution although the spectral plots shown in Supporting Figure S1 still confirm the presence of a significant FRET process. We attribute this difference to changes in the dyes absorption/emission properties due to the large amount of DMSO present which would alter its solvation and dielectric properties. Overall these data still strongly suggest that the peptide assembles to the QDs and allows for proximity-dependent FRET in the presence of increasing concentrations of DMSO. To strike a balance between the need for DMSO dissolution and for buffering capacity, we typically used 65% DMSO unless otherwise indicated in the subsequent experiments.

In a second control experiment, self-assembly of C_{60} to the QD surface *via* the pepC_{60} conjugate was confirmed by monitoring changes in the assembled QD hydrodynamic size with dynamic light scattering (DLS) before and after exposure to the peptide.

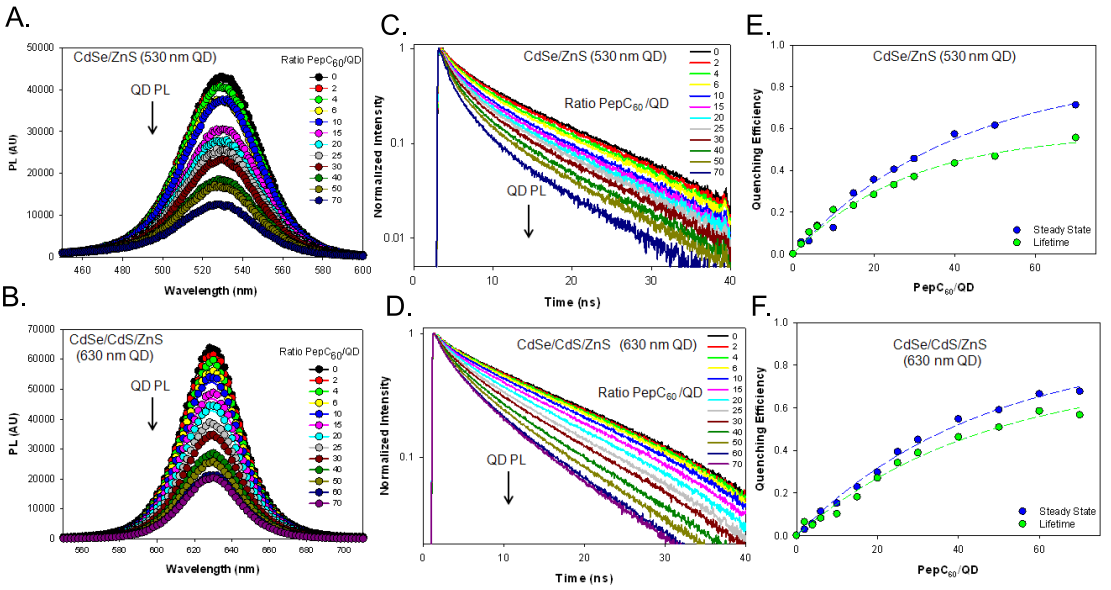

Figure 3. Steady-state PL and excited-state lifetime analysis from select QD−$(pepC_{60})_N$ conjugates. Representative PL spectra collected from (A) 530 nm QDs and (B) 630 nm QDs assembled with the indicated increasing ratios of $pepC_{60}$. Samples were excited at 300 nm. Representative, normalized time-resolved PL decay data collected from (C) 530 nm QDs and (D) 630 nm QDs assembled with the indicated ratios of $pepC_{60}$. Samples were excited at 375 nm. Comparison of normalized quenching profiles from steady-state versus time-resolved PL decay data from (E) 530 nm QDs (F) 630 nm QDs versus increasing ratio of $pepC_{60}$ assembled per QD. Normalized steady-state data are plotted in blue while the corresponding time-resolved PL decay quenching is shown in green.

Figure 2C shows DLS data for 630 nm QDs under three different conditions. First, the hydrodynamic sizes of 630 nm QDs in water and in 65% DMSO (aq) were compared. The QD hydrodynamic diameter (D_H) measured in water was smaller than in 65% DMSO, 14.1 and 18.9 nm, respectively, which reflects changes in the hydration layer in different solvents. As expected, the hydrodynamic size of 630 nm QDs is larger than the hard diameter of the semiconductor components as measured by TEM, 7.7 ± 0.5 nm (see SI Figure S8). Importantly, the D_H for 630 nm QDs in 65% DMSO increased from 18.9 to 26.3 nm after being assembled with 40-$pepC_{60}$. A D_H value for the neat $pepC_{60}$ could not be measured because its size was smaller than the minimum resolvable with our instrument. The DLS results, combined with the data in Figure 2A, provide confirmation that $pepC_{60}$ conjugates can successfully self-assemble to QD surfaces in solutions with relatively high concentrations of DMSO.

In the third and final control experiment, PL quenching of 550 nm QDs in 75% DMSO solutions was tested with free C_{60}-pyrrolidine tris-acid and $pepC_{60}$ to determine if the peptide significantly enhanced QD quenching. The results are summarized in Figure 2D; the corresponding steady-state PL spectra are shown in the SI Figure S2. A complex bimodal decay profile for QD PL was observed with increasing ratios of $pepC_{60}$ per QD, where a continuous and dynamic quenching was observed across all the ratios of $pepC_{60}$ tested. At a ratio of $N = 75$ peptides, almost two-thirds of the QD PL was quenched (~32% QD PL remaining). This is in stark contrast to the minimal, linear quenching observed with the same increasing ratios of free C_{60}-pyrrolidine tris-acid per QD added in the same buffer. For example, the 550 nm QD PL was quenched by ~28% with only $N = 10$ equiv of $pepC_{60}$, and this level was not even achieved with up to $N = 150$ equiv free C_{60}-pyrrolidine tris-acid.

Previous reports have suggested that similarly sized 550 nm DHLA-coated QDs can be decorated with an average of 50 ± 10 His_6 peptides on their surface.[41] In support of this putative maximum assembly ratio, the apparent quenching response observed for the $pepC_{60}$ conjugates suggests an underlying bimodal process with an inflection point around a ratio of $N = 50$ peptides; the fit for 0 to 50 peptides is quite steep in Figure 2D while that for the subsequent $N \geq 50$ to 150 peptides closely resembles the slope of the linear quenching by neat C_{60}-pyrrolidine tris-acid. This would correspond to a high initial rate of quenching expected for $pepC_{60}$ directly attached to the QDs along with a subsequent much weaker, linear-quenching process driven by Stern−Volmer solution-phase collisional quenching interactions. Cumulatively, the results from the control experiments establish two important points: (i) $pepC_{60}$ are capable of efficient self-assembly to QDs in 50−75% DMSO (as shown with the Cy3-labeled peptide in Figure 2A, and SI Figures S1/S2 along with DLS in Figure 2C), and (ii) $pepC_{60}$-QD attachment results in a far more pronounced rate of QD quenching, indicating a critical role for proximity between the QD and C_{60} (Figure 2D).

TABLE 2. QD Excited State Lifetimes Collected from QD−(pepC$_{60}$)$_N$ Conjugates[a]

	530 nm QD		550 nn QD		580 nm QD		630 nm QD	
pepC60/QD (*N*)	τ_{Av}	% quenching	τ_{Av}	% quenching	τ_{Av}	% quenching	τ_{Av}	% quenching
0	9.13 ± 0.04	0	11.68 ± 0.04	0	8.95 ± 0.04	0	17.52 ± 0.04	0
2	8.70 ± 0.04	5	11.18 ± 0.04	4	8.08 ± 0.03	10	16.40 ± 0.04	6
4	8.18 ± 0.04	10	10.96 ± 0.04	6	7.67 ± 0.03	14	16.66 ± 0.04	5
6	7.93 ± 0.04	13	10.78 ± 0.04	8	7.38 ± 0.03	18	16.10 ± 0.04	8
10	7.20 ± 0.04	21	10.55 ± 0.04	10	6.67 ± 0.03	25	15.74 ± 0.04	10
15	7.01 ± 0.04	23	10.26 ± 0.04	12	5.90 ± 0.03	34	14.35 ± 0.04	18
20	6.54 ± 0.04	28	9.90 ± 0.04	15	5.12 ± 0.03	43	12.79 ± 0.03	27
25	6.11 ± 0.04	33	9.80 ± 0.04	16	4.41 ± 0.02	51	11.54 ± 0.03	34
30	5.75 ± 0.04	37	9.36 ± 0.03	20	3.65 ± 0.03	59	10.71 ± 0.03	39
40	5.17 ± 0.03	43	9.09 ± 0.03	22	2.85 ± 0.02	68	9.42 ± 0.03	46
50	4.86 ± 0.04	47	8.71 ± 0.03	25	2.46 ± 0.02	73	8.61 ± 0.03	51
60	—	—	8.28 ± 0.03	29	2.14 ± 0.02	76	7.28 ± 0.02	58
70	4.05 ± 0.04	56	7.89 ± 0.03	32	2.02 ± 0.02	77	7.60 ± 0.03	57

[a] QD decay profiles fitted with a biexponential function. Averaged lifetime values are amplitude weighted.

Steady-State and Excited State QD PL versus Increasing Ratios of PepC$_{60}$. Satisfied with the performance of His$_6$-based self-assembly in this system, we began our photophysical analysis by self-assembling increasing ratios (N = 2−70) of pepC$_{60}$ to three colors of DHLA-coated type I CdSe/ZnS QDs outlined in Table 1 and monitored the changes in PL spectra and intensities. The upper ratio of 70 was chosen so as to consistently ensure saturation of the QD surface.[41] Figure 3A shows representative steady-state PL spectra collected from the 530 nm QDs (spectra for the 550 and 580 nm QDs can be found in SI Figure S3). The degree of exciton quenching clearly increases with the number of pepC$_{60}$ assembled per QD. Next, we self-assembled increasing ratios of pepC$_{60}$ to the DHLA-coated 630 nm CdSe/CdS/ZnS QDs, where a similar increase in exciton quenching was observed with increased pepC$_{60}$ per QD (Figure 3B). Both of the QD samples in Figure 3A−B reach ∼70% quenching at a loading of ∼70 peptides per QD.

In addition to steady-state analysis, Figure 3C−D show normalized PL lifetime decay curves for the 530 and 630 nm QDs, respectively (see SI Figure S3 for decays for the 550 and 580 nm QDs). The QD PL decay curves were fit with a biexponential function, and the average lifetimes (τ_{av}) are shown in Table 2. The lifetime components (τ_1 and τ_2) and their corresponding fractional amplitudes are summarized in the SI Table S1. We note that in all cases the fractional amplitude of the longer lifetime component (τ_1) decreases as the exciton is quenched while the fractional amplitude of the shorter lifetime component (τ_2) increases. Consistent with the steady-state results, the average exciton lifetimes (τ_{Av}) decrease with increasing pepC$_{60}$ assembled per QD. A comparison of the QD quenching efficiency derived from steady-state and time-resolved PL data is shown in Figure 3E−F for the 530 and 630 nm QDs, respectively (see SI Figure S3 for analogous data for the 550 and 580 nm QDs). Overall, data for all four QD samples tested had quite similar quenching kinetics. The steady-state and lifetime decay quenching curves generally tracked each other as a function of the number of pepC$_{60}$ assembled per QD for the 530 and 630 nm emitting QDs, although this was not a one-for-one imposition of data. Quenching curves for the 550 and 580 nm QDs did not track as closely (SI Figure S3), with the steady-state quenching being more pronounced, suggesting the presence of more complex underlying kinetic processes. Further, in all cases the steady state PL quenching manifested a consistent and slightly more intense level of quenching efficiency than the lifetime decay.

Ultrafast Transient Absorption Spectroscopy. The excited state dynamics of CdSe and CdS QDs have been previously examined under various conditions and solvents using TA spectroscopy.[42−44] Direct photoexcitation of the QD results in a ground state bleach of the 1S state that occurs within hundreds of femtoseconds followed by a multiexponential recovery that is attributed to conduction band (CB) filling and surface trapping of charges that persist on the nanosecond to microsecond time scale. When no acceptor is present, the lowest energy allowed exciton transition is the 1S3/2(h)−1S1/2(e), denoting a hole in the 1S3/2 level of the valence band (VB) and an electron in the 1S1/2 level of the conduction band. The predominant spectral features attributed to the 580 nm QD sample exciton state are observable at 480 and 575 nm, as negative features. A kinetic fit at these wavelengths reveal a triexponential recovery of the ground state (see SI Table S2).

Figure 4 shows representative fsTA spectra and kinetics for the neat 580 nm QDs, neat pepC$_{60}$, and 20:1 and 80:1 pepC$_{60}$:QD assemblies. The latter ratio was again chosen to ensure QD surface saturation. Figure 4A−B are overlaid spectra collected at the indicated probe delay times, and Figure 4C−D show the pep*C$_{60}$ (photoexcited sample) and 580 nm QD ground state bleach kinetics monitored at 480 and 505 nm,

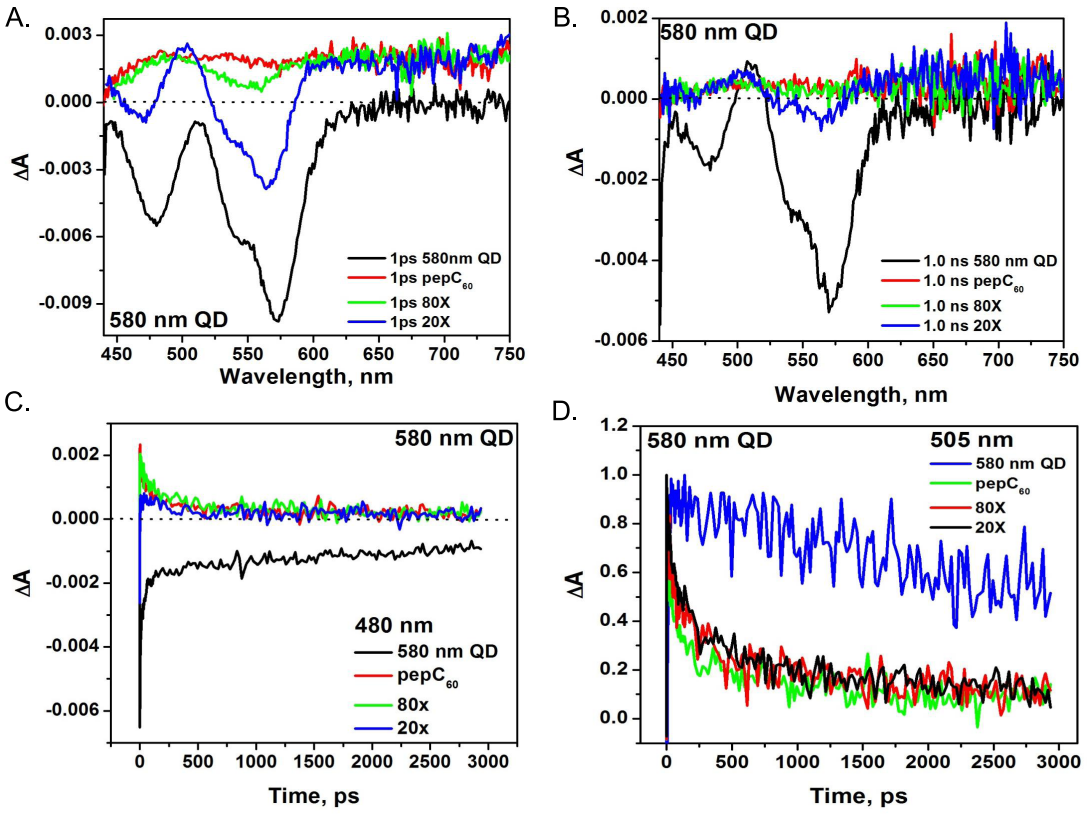

Figure 4. Transient absorption spectra. Superimposed time-resolved transient absorption spectra of 580 nm QDs (black), 8 μM pepC$_{60}$ (red), QD-(pepC$_{60}$)$_{20}$ (blue-20×), and QD-(pepC$_{60}$)$_{80}$ conjugates (green-80×) at (A) 1 ps and (B) 1016 ps following excitation with a 420 nm laser pulse. Changes in bleach kinetics over time for each sample as monitored at (C) 480 nm and (D) 505 nm.

respectively. These data reveal two principal features: (i) upon the addition of pepC$_{60}$, the ground state bleach of the QD is quenched, and this quenching process is concentration dependent; and (ii) the lifetimes and spectral features of the QD quenching product are nearly identical to that of pepC$_{60}$ alone. These findings are consistent with a QD quenching that arises from energy transfer and that changes in concentration, surface loading, ratio, and pepC$_{60}$/QD electronic coupling are sensitive parameters that can modulate QD quenching.

Upon the addition of pepC$_{60}$, the negative peak at 480 and 575 nm attributed to the QD ground state bleach is quenched immediately after the 120 fs laser pulse as is shown at a 1 ps laser delay time in Figure 4A. This graph also illustrates that higher concentrations of pepC$_{60}$ translates to more QD ground state quenching on this ultrafast time scale. The resulting transient signal upon quenching appears nearly identical to pep*C$_{60}$ collected alone. In this case, photoexcitation of pepC$_{60}$ results in pep*C$_{60}$ and emerges as a positive, broad band absorption from 450−750 nm. The photophysics of both substituted and unsubstituted C$_{60}$, as well as the radical anion, have been widely studied,[45−48] and the salient features near 500 nm are similar to that of the pep*C$_{60}$, with a broad absorption from 350−520 nm.[48] However, the spectral signature of the C$_{60}$ radical anion is typically observed in the NIR from 900−2000 nm, which could not be measured in these experiments.[13,22] These spectra are consistent with an energy transfer process from the QD to pepC$_{60}$ occurring as a competing mechanism for excitonic quenching. Since photoexcitation is primarily into the QD at 420 nm and away from the peak C$_{60}$ absorbance, we do not expect to observe a significant contribution of pep*C$_{60}$ generated from the initial laser pulse until the highest loadings for any of the QD samples (see SI Figure S9). A kinetic analysis at key wavelengths from both the ground state bleach of the QD and from the pep*C$_{60}$ show two features: (i) a fast quenching of the QD; and (ii) spectral feature and decay times associated with pep*C$_{60}$ are identical to the product of quenching, namely, the energy transfer product, pep*C$_{60}$. These two points are illustrated in Figure 4C−D, in the kinetic overlay of pepC$_{60}$, QD, and pepC$_{60}$:QD assemblies. We also note some similarity between this data set and the previously mentioned study that coupled QDs to a redox-active Os-complex where FRET from the QD to the metal complex was ascribed as the primary quenching mechanism.[38]

DISCUSSION AND CONCLUSIONS

As mentioned initially, a number of QD−C$_{60}$ constructs have been assembled and interrogated in pursuit of understanding photoexcited ET in these systems. Within these systems, the observed QD PL

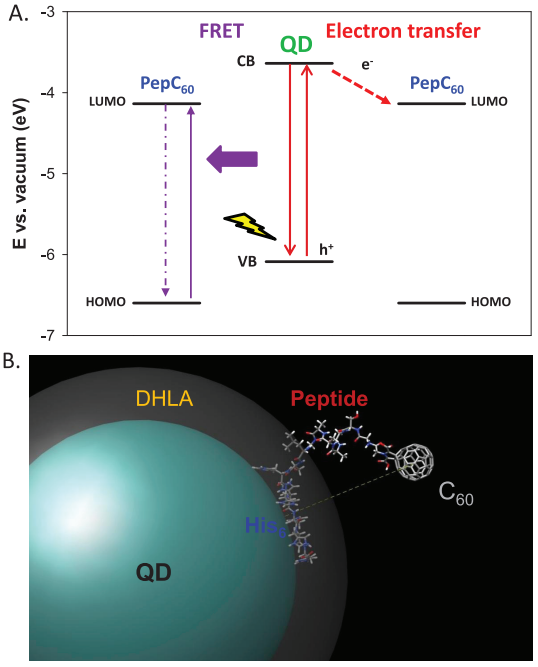

Figure 5. Relative energy levels estimated for the pepC$_{60}$ and QDs along with a model of a QD-pepC$_{60}$ assembly. (A) Schematic representation of CdSe/ZnS conduction band (CB) and valence band (VB) relative to the pepC$_{60}$ lowest unoccupied molecular orbital (LUMO) along with putative pathways for both the FRET and ET QD quenching pathways. (B) Model of a QD assembled with one pepC$_{60}$. The blue sphere represents a QD with a radius of 30 Å (~550 nm QD) with a DHLA ligand shell shown in light gray, which extends ~11 Å from the QD surface. In the partially folded peptide conformation shown, the distance from the QD center to the center of the C$_{60}$ is ~56 Å. A fully extended peptide (not shown) would result in the QD-C$_{60}$ separation of 63−64 Å while a fully folded conformation would place the C$_{60}$ acceptor at (or in) the QD surface; a distance that should correspond to the core/shell radius for each QD sample.

quenching has been primarily attributed to ET from the photoexcited QD to the C$_{60}$.[13,14,22,24,25] We therefore begin by considering this quenching mechanism with the pepC$_{60}$ used in this study. Differential pulse voltammetry (DPV) was used to measure the reduction potential of C$_{60}$-pyrrolidine tris-acid and pepC$_{60}$ to determine if peptide labeling altered the fullerene's intrinsic electrochemistry (see SI Figure S4). Two distinct reduction waves were measured for both C$_{60}$-pyrrolidine tris-acid and pepC$_{60}$ in the electrochemical window scanned (0 to −1.2 V vs Ag/AgCl). The unmodified C$_{60}$-pyrrolidine tris-acid reduction potentials were at E_1 = −61 mV and E_2 = −89 mV. Similarly, the measured reduction potentials for pepC$_{60}$ were at E_1 = −50 mV and E_2 = −84 mV. This indicates that covalent coupling of the peptide to C$_{60}$-pyrrolidine tris-acid only shifts the fullerene's first reduction potential by 11 mV, thus retaining the strong electron accepting property of the fullerene.

The pepC$_{60}$ reduction potential (E_1 = −50 mV) measured by DPV was used to estimate[49] the electron affinity (E_a), −4.1 eV versus vacuum (−4.3 eV using onset potential), which agrees well with the lowest unoccupied molecular orbital (LUMO) energies for C$_{60}$ (−4.3 eV) reported in the literature.[13] To compare the pepC$_{60}$ LUMO with the QDs, the CB and VB energy levels for CdSe/ZnS QDs (2.2 nm diameter core with ~3.5 monolayers of ZnS) were estimated from the reduction and oxidation potentials, respectively, also as reported in the literature.[50] The relative energy levels for the QD CB and VB are shown relative to the pepC$_{60}$ LUMO in Figure 5A. Clearly, photoexcited electrons in the QD CB are energetically allowed to transfer to the LUMO of pepC$_{60}$; this process would also be consistent with the faster bleach recovery in the QD−pepC$_{60}$ conjugates compared to the QDs alone, shown in Figure 4. The minimization of pep*C$_{60}$ generation at lower ratios where significant quenching is still noted across all samples also suggests that reverse ET from the pep*C$_{60}$ to the QD can be excluded. Due to the similar LUMO energies between pepC$_{60}$ and C$_{60}$, we assume that the highest occupied molecular orbital (HOMO) of pepC$_{60}$ will not be drastically different from C$_{60}$ and use a reported value of ~6.60 eV.[14] As a result, hole transfer from the QD to pepC$_{60}$ is energetically forbidden as a quenching mechanism. The DPV and fsTA results help simplify the following analysis by confirming that QD quenching is (i) primarily by a rapid energy transfer process, (ii) that occurs from the QD to the C$_{60}$, and (iii) the complication of hole transfer from the QD to the C$_{60}$ is not included in this process.

While this analysis provides strong evidence that QD exciton quenching by ET is energetically feasible, other potential quenching mechanisms still cannot be overlooked. As shown in Figure 1C, the optical absorption tail of pepC$_{60}$ extends through most of the visible spectrum, suggesting that FRET may also play a role in the luminescence decay mechanism of the QD−(pepC$_{60}$)$_N$ complexes. A FRET based analysis shows that the overlap integrals between the QDs and pepC$_{60}$ range from 0.96 × 10^{-14} cm^3 M^{-1} for the 630 nm QDs with the least spectral overlap to 1.88 × 10^{-14} cm^3 M^{-1} for the 530 nm QDs with the largest spectral overlap. The spectral overlap integrals yield relatively short Förster distances ranging from 24 to 30 Å. In order to obtain predicted center-to-center separation distances for these complex constructs, structural models of the QD−pepC$_{60}$ assembly were prepared (see Materials and Methods); a one-to-one construct is shown in Figure 5B. As shown in Table 1, the predicted center-to-center separation distances are larger than the R_0 values for 50% energy transfer efficiency for a single QD donor and a single pepC$_{60}$ acceptor. While the model shows a potential "snapshot" of the center-to-center QD−C$_{60}$ separation distance (~56 Å) based on a specific peptide conformation, in reality the peptide is flexible and may achieve numerous conformations, although direct contact with the QD surface is not favored.

One important factor that is intrinsic to our assemblies, and which may serve to make FRET a more

TABLE 3. Estimated FRET and ET Rate Constants (s^{-1}) for the QD−$(pepC_{60})_N$ Conjugates

	530 nm QD			550 nm QD			580 nm QD			630 nm QD		
$pepC_{60}$/QD (N)	k_{total}	k_{FRET}	k_{ET}[a]	k_{total}	k_{FRET}	k_{ET}	k_{total}	k_{FRET}	k_{ET}	k_{total}	k_{FRET}	k_{ET}
0	1.1×10^8			8.6×10^7			1.1×10^8			5.7×10^7		
2	1.1×10^8	2.5×10^6	2.1×10^5	8.9×10^7	5.4×10^5	1.4×10^6	1.2×10^8	5.0×10^5	5.5×10^6	6.1×10^7	5.0×10^4	1.9×10^6
4	1.2×10^8	2.5×10^6	6.4×10^5	9.1×10^7	5.4×10^5	8.7×10^5	1.3×10^8	5.3×10^5	4.1×10^6	6.0×10^7	4.9×10^4	6.9×10^5
6	1.3×10^8	2.5×10^6	2.4×10^5	9.3×10^7	5.4×10^5	6.5×10^5	1.4×10^8	5.4×10^5	3.4×10^6	6.2×10^7	5.1×10^4	7.9×10^5
10	1.4×10^8	2.6×10^6	3.7×10^5	9.5×10^7	5.4×10^5	3.8×10^5	1.5×10^8	5.9×10^5	3.2×10^6	6.4×10^7	5.2×10^4	5.9×10^5
15	1.4×10^8	2.4×10^6	—	9.7×10^7	5.4×10^5	2.5×10^6	1.7×10^8	6.5×10^5	3.2×10^6	7.0×10^7	5.7×10^4	7.8×10^5
20	1.5×10^8	2.4×10^6	—	1.0×10^8	5.5×10^5	2.2×10^5	2.0×10^8	7.4×10^5	3.4×10^6	7.8×10^7	6.4×10^4	9.9×10^5
25	1.6×10^8	2.4×10^6	—	1.0×10^8	5.4×10^5	1.2×10^5	2.3×10^8	8.4×10^5	3.8×10^6	8.7×10^7	7.0×10^4	1.1×10^6
30	1.7×10^8	2.3×10^6	—	1.1×10^8	5.5×10^5	1.6×10^5	2.7×10^8	1.0×10^6	4.4×10^6	9.3×10^7	7.5×10^4	1.1×10^6
40	1.9×10^8	2.3×10^6	—	1.1×10^8	5.4×10^5	7.3×10^4	3.5×10^8	1.2×10^6	4.7×10^6	1.1×10^8	8.5×10^4	1.1×10^6
50	2.1×10^8	2.2×10^6	—	1.1×10^8	5.3×10^5	5.0×10^4	4.1×10^8	1.4×10^6	4.5×10^6	1.2×10^8	9.2×10^4	1.1×10^6
70	2.5×10^8	2.2×10^6	—	1.3×10^8	5.4×10^5	4.8×10^4	5.0×10^8	1.6×10^6	3.9×10^6	1.3×10^8	1.0×10^5	9.6×10^5

[a] Values not shown (—) are negative and considered unphysical.

favorable process, is the ability to centrosymmetrically array an increasing number of $pepC_{60}$ acceptors around each QD. Although the spectral overlap between a QD donor with a single C_{60} acceptor is relatively small, arraying an increasing number of such acceptors around the QD essentially functions to proportionally increase the FRET acceptor absorption cross section. This has the net effect of increasing the probability that FRET will occur from the photoexcited QD to one of the surrounding C_{60} acceptors. This very same effect is consistently noted in almost all other single QD donor-multiple dye acceptor FRET configurations.[6,51] The compact DHLA coating on the QD surface (shown in light gray, Figure 5B) provides the only steric barrier that could limit the QD/C_{60} separation distance to ~11 Å from the QD surface, allowing for a range of reasonable separation distances that would not preclude FRET. Additionally, even if the peptide conformation was fully extended, this would not preclude FRET, as the C_{60} separation distance from the QD core would not increase that significantly. For example, in the model shown in Figure 5B, which roughly corresponds to a 530−550 nm emitting CdSe/ZnS QD, a fully extended peptide conformation would place the C_{60} at a distance of ~63−64 Å from the QD center which should yield ~1.5% FRET E for a single donor-single acceptor configuration. However, FRET E quickly becomes nontrivial with many acceptors even at this separation distance and can increase to ~44% for a ratio of 50 acceptors/QD. Moreover, the data in Figure 3A−B show significant QD PL quenching (30−40%) beginning to appear at ratios of 10−20 acceptors per QD, suggesting a closer putative separation distance if FRET were the sole quenching mechanism.

It is also important to note that arraying an increasing number of $pepC_{60}$ acceptors around the central QD would similarly enhance the possibility of ET as well. One caveat to this enhancement is the issue of competitive excitation light absorption by the acceptor, especially when high ratios of $pepC_{60}$ are displayed around the QD. Although the absorption of one or a small number of acceptors is relatively low compared to that of a QD (see extinction coefficients in Table 1), the cumulative increase from assembling ~50−60 acceptors around a single QD can be quite significant and this may also need to be considered in certain circumstances (see SI Figure S9 for some estimates on competitive absorption). We note that this can also be minimized by selecting a wavelength that predominantly excites the QD, as done here. Overall, the possibility for increased FRET/ET as a function of acceptor ratio suggests a decisive contribution may be provided by the presence/absence of spectral overlap within the system.

Since data and theory support the potential for both FRET and ET quenching mechanisms, we derived a simple mathematical model (for derivation, see Energy Transfer Kinetic Analysis in the Materials and Methods) to simulate the putative FRET and ET contributions to the total quenching observed for each QD when assembled with increasing numbers of $pepC_{60}$. The model accounts for underlying variables such as spectral overlap, separation distance, and acceptor number and assumes that the observed QD quenching is a result of the four different potential decay mechanisms: radiative, nonradiative, FRET, and ET. Nanosecond lifetime quenching studies are used to estimate the theoretical FRET and ET efficiencies; however, the model does not account for the specific type of ET (*i.e.*, hopping, tunneling, superexchange, *etc.*). It is important to note that such models have been used previously in an analogous manner to understand the energy transfer kinetics in similar QD carbon allotrope constructs.[26,27] Using this model, the FRET and ET rates were calculated and are summarized in Table 3, assuming that FRET and ET are the only relevant quenching mechanisms. The dichotomy between the two different quenching mechanisms is highlighted by examining the rates for the smallest and largest QD systems.

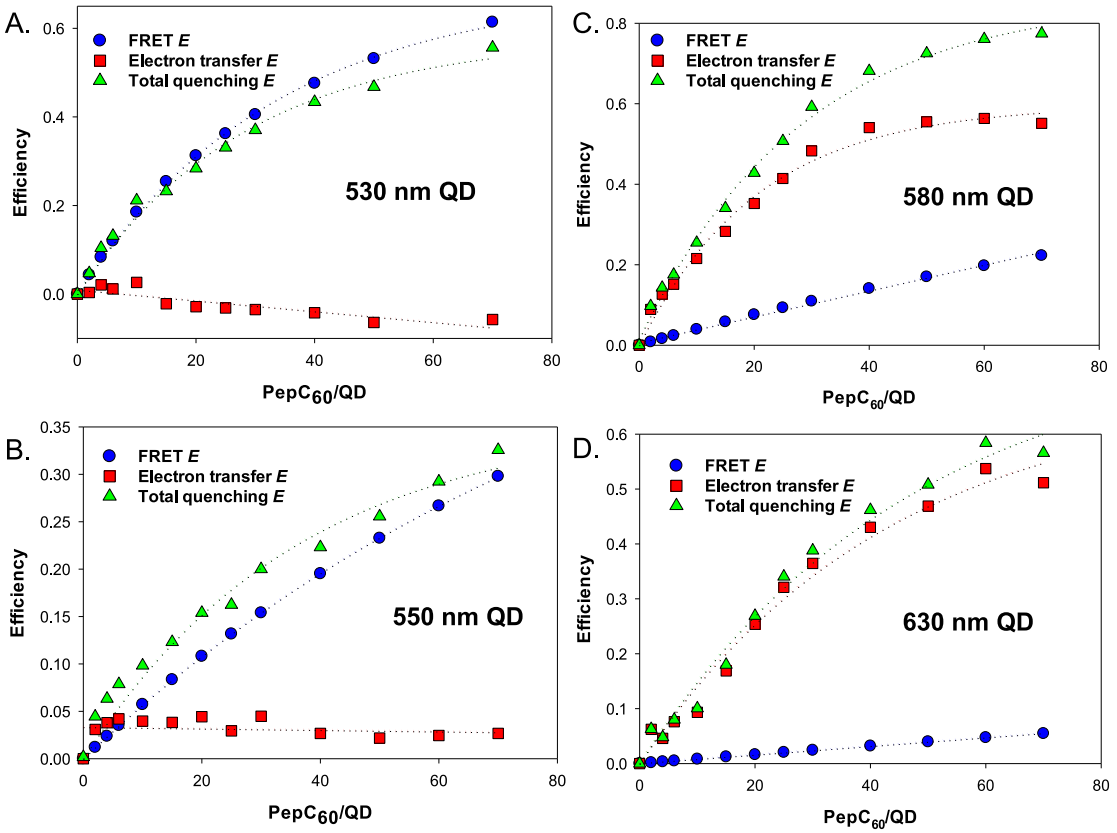

Figure 6. Relative FRET/electron transfer components. The relative FRET and electron transfer (ET) efficiencies estimated for the (A) 530 nm, (B) 550 nm, (C) 580 nm, and (D) 630 nm QDs versus increasing ratios of pepC$_{60}$ acceptor displayed.

The 530-nm-emitting QD−(pepC$_{60}$)$_N$ has the largest putative FRET rate constant (2.4×10^6 s^{-1}, $N = 20$) and a negligible ET rate, consistent with the largest underlying donor−acceptor spectral overlap and the shortest separation distance. In contrast, the 630 nm emitting QD−(pepC$_{60}$)$_N$ system has a relatively small estimated FRET rate constant (6.4×10^4 s^{-1}, $N = 20$) but a large estimated ET rate constant (9.9×10^5 s^{-1}, $N = 20$), indicating that resonant energy transfer was much slower or more unfavored than photoexcited ET within this system. We note that this result is mechanistically similar to that reported by Bang and Kamat, where the photocurrent in their QD−C$_{60}$ system was highest for the larger size QDs tested.[13] Overall, the FRET rates go down with increasing QD size and a decrease in spectral overlap across Table 3, while the ET rate increases, consistent with the transition from a more dominant FRET process to the more dominant ET.

Figure 6 plots the total experimental quenching efficiency along with the calculated FRET and ET components for the 530 through 630 nm QD−(pepC$_{60}$)$_N$ constructs, respectively. For the smaller QD systems, FRET E closely follows the total quenching efficiency suggesting that it is the dominant process. Indeed the ET efficiencies for the smaller 530 nm QD yield some negative values for $N > 15$, which are not physically valid. Similarly, the FRET E is significantly larger than ET for the 550 nm QD−(pepC$_{60}$)$_N$ complexes. These results strongly suggest that the deactivation of the 530 and 550 nm QD−(pepC$_{60}$)$_N$ complexes may be dominated by FRET. Distinct differences between the quenching mechanisms present can be found in the 580 and 630 nm QD−(pepC$_{60}$)$_N$ constructs, and these are used here as illustrative examples. Figure 6C shows the plots derived from the 580 nm QD−(pepC$_{60}$)$_N$ data, where ET efficiency is larger than the estimated FRET efficiency, although the latter is still present and significant. Figure 6D suggests that ET should dominate the deactivation of the 630 nm QD−(pepC$_{60}$)$_N$ complexes. The reduction in the FRET efficiency here is assumed to result from a combination of the decrease in the spectral overlap, and the corresponding value of R_0, as well as a contribution from an increase in the QD−C$_{60}$ separation distance (Table 1). These plots suggest that as the size of the QD is increased and the PL band shifts to longer wavelengths, a significant reduction in the FRET efficiency occurs while a high level of overall quenching is still achieved because ET is still an active and available alternative "fall-back" or secondary quenching mechanism. Importantly, the plots in Figure 6C,D suggest that there should be a small but still significant quenching component attributable to FRET in the 580 nm QD system, whereas FRET should be almost nonexistent in the 630 nm QD

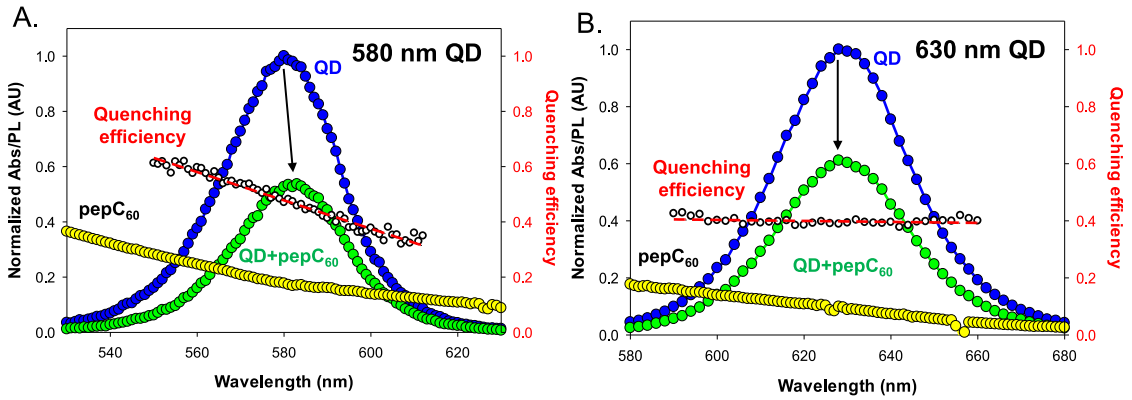

Figure 7. Wavelength dependent QD quenching profiles. PL spectra for the (A) 580 nm and (B) 630 nm QDs alone and when assembled with 25-pepC$_{60}$ acceptors. Samples were excited at 300 nm. Results of a wavelength dependent quenching analysis are also shown. The normalized pepC$_{60}$ acceptor absorption profile is shown in each of the plots superimposed over the data. Note the asymmetric profile for the red-shifted 580 nm QDs assembled with pepC$_{60}$ acceptors.

system. As a final analysis to confirm these predictions, we undertook a wavelength dependent FRET quenching analysis of the QD PL profiles collected from these two redder QD samples.

As Pons et al. previously demonstrated, the FRET rate between QD donors and broadly absorbing acceptors is wavelength dependent.[52] This behavior arises from the fact that the ensemble Gaussian QD PL profile is, in reality, made up of a continuum of slightly different-sized QDs that emit at slightly different wavelengths with individual PL emission line widths that are significantly narrower (~15 nm) than the overall ensemble spectrum. The QD FRET rate in this configuration is thus a function of both the QD PL at a discrete wavelength and the acceptor extinction coefficient at that wavelength, and can be estimated as described in the Materials and Methods. The presence of wavelength dependent QD quenching in a QD donor–acceptor system serves to provide strong evidence of an underlying FRET process,[38] while its absence can suggest the presence of other quenching mechanisms.[53] Figure 7A shows representative data from this analysis for the 580 nm QD sample without the acceptor and as assembled with 25 pepC$_{60}$ acceptors. Here, a linear rate of QD quenching is found within the QD-(pepC$_{60}$)$_{25}$ PL that increases toward the blue portion of the spectrum and which directly follows the normalized pepC$_{60}$ absorption profile shown superimposed over the spectra. The QD–(pepC$_{60}$)$_{25}$ PL also clearly manifests an asymmetrical red-shifted spectrum that would be expected for a QD ensemble engaged in such a wavelength-dependent quenching process. Similar wavelength-dependent quenching profiles which tracked with the pepC$_{60}$ absorption were also observed within the 530 and 550 nm QD–pepC$_{60}$ systems (data not shown). Figure 7B shows representative data collected from the 630 nm QD system in the absence/presence of 25-pepC$_{60}$ acceptors. In contrast to the previous example, appreciable wavelength dependent quenching was not observed in this system at this or any acceptor ratio (data not shown). Moreover, the quenched QD profile does not present any visible red-shifted asymmetry. Cumulatively, these results serve as a strong confirmation that a FRET quenching process is present in the 530, 550, and 580 nm QD systems, but not in the 630 nm QD assemblies. These data also provide strong corroborating evidence for the predictions made by the above model.

Overall, these results suggest that the competition between FRET- and ET-based quenching in the QD–(pepC$_{60}$)$_N$ assemblies is dependent on a complex interplay of several factors including the QD emission maximum/quantum yield effects on the resulting spectral overlap, QD size and its effect on the QD-pepC$_{60}$ donor–acceptor separation, and the number of acceptors arrayed per QD. Although both processes are permitted, FRET appears to be more favored when sufficient spectral overlap is present. Clearly, one way to avoid dual or competing energy transfer quenching mechanisms in hybrid QD/C$_{60}$ systems is to eliminate FRET by pairing the C$_{60}$ with QD donors that emit in the near-infrared, resulting in no underlying spectral overlap. Indeed, these criteria were met in an elegant study that demonstrated size-dependent electron transfer from PbS QDs to fullerenes.[15] It is not surprising that FRET could be responsible for (type I and quasi type II) QD quenching by C$_{60}$ acceptors given the growing number of reports where more than one energy transfer pathway was deemed responsible for QD PL quenching by other carbon-based allotropes.[26–31] For example, Brus and co-workers investigated the potential for FRET and ET between CdSe/ZnS QDs and graphene sheets by analyzing QD blinking kinetics on quartz and graphene substrates.[28] In their system, they discovered that resonant energy transfer was much faster than photoexcited electron transfer, similar to our results in Table 3. Lightcap and Kamat also investigated the dual contributions of FRET and ET responsible for QD quenching in systems composed of CdSe QDs and graphene oxide (GO) and reduced

graphene oxide (RGO).[26] They showed that under certain conditions both FRET and ET contributed to fluorescence quenching, but after prolonged irradiation and charging of the GO, FRET became the main pathway for nonradiative excited state decay of the QDs. The potential competition between FRET and charge transfer was also evaluated in systems composed of QDs coupled to double-walled carbon nanotubes (DWNTs).[27] This study found that CdSe core only QDs were quenched *via* a charge transfer-based mechanism, whereas CdSe/ZnS core/shell QDs engaged in resonance energy transfer with the DWNTs.

Although considerable progress has been made on developing methods to controllably attach various donors and other molecules to carbonaceous materials, this generally remains quite challenging.[20] The unique properties provided by peptide-driven metal affinity coordination to the QDs helped overcome many of these issues and provided for exceptional control over C_{60} acceptor valency with the four different QD samples used here. In particular, the ratiometric control achieved here allowed us to examine the systems at different states of efficiency. We also note that this "biological" approach unexpectedly allowed us to controllably bridge or attach two disparate nanoparticulate materials to each other in a mixed organic/aqueous system. This demonstration shows that biological molecules can be used to assemble complex nanoheterostructures and suggests that other hybrid nanostructures, which may initially appear to be incompatible with aqueous conditions, can be assembled and interrogated in a similar manner. A covalent linkage or some functional bridging equivalent (*i.e.*, coordination of the peptide to the QD surface) has been suggested as a critical requirement for efficient or enhanced ET in these systems. Indeed, Bang and Kamat investigated several QD−C_{60} nanoconstructs for applications in QD-based solar cells and found that linking C_{60} to the QDs *via* alkylthiol ligands could enhance the photocurrent generation process.[13] ET through space is highly distance dependent and typically manifests an exponential decay with rates decreasing by an order of magnitude for each 1.5−2.0 Å in separation distance.[54,55] The current results suggest that peptide linkages provide efficient ET pathways for properly designed QD−C_{60} constructs and that, given the separation distances, such ET may proceed by tunneling or hopping, although confirmation of a specific mechanism is beyond our current scope. This does, however, suggest the possibility of redesigning the peptide linkage and length to optimize ET and the potential to use this type of system to understand ET processes and their distance dependence within the peptides themselves.[54,55]

Energy transfer with QD donors can sometimes be complex and has been found to result from unexpected pathways. For example, a systematic examination of QD interactions with a redox-active osmium polypyridyl acceptor complex found the energy transfer to be almost exclusively attributable to FRET despite very weak underlying spectral overlap.[38] Previous reports have also highlighted the complexity of energy transfer interactions in hybrid systems composed of QDs and carbon allotropes.[26−31] The current report corroborates the potential for both FRET and ET deactivation pathways occurring in the photoexcited QD−C_{60} system based upon a complex interplay of several inherent factors. If sufficient QD−C_{60} spectral overlap is present and the separation distance and acceptor ratio allow for it, then FRET may dominate. As shown here, the FRET rate will also track as a function of spectral overlap/acceptor ratio. If not, and if sufficient distance or a linkage is available, ET appears to be the 'default' quenching process, which is not surprising given the excellent electron acceptor properties of C_{60}. Clearly both quenching processes should be carefully considered when analyzing similar QD−C_{60} architectures, especially for energy conversion purposes.[56] As such, these results have important implications for developing new hybrid QD-carbon based materials and sensors along with optimizing QD donor/C_{60} acceptor systems for energy conversion applications.[9]

MATERIALS AND METHODS

Quantum Dots. CdSe/ZnS QDs ($\lambda_{em\text{-}max}$ = 530, 550, and 580 nm) were synthesized *via* a hot-injection method according to published procedures.[57] CdSe/CdS/ZnS QDs ($\lambda_{em\text{-}max}$ = 630 nm) were prepared as previously reported[58] using a modified protocol relying on the successive ion layer adsorption and reaction (SILAR)[59] with a thermal cycling[60,61] technique. The native, hydrophobic coatings on the QD surfaces were replaced with dihydrolipoic acid (DHLA) premetalated with zinc as reported,[62] to yield hydrophilic QDs coated with DHLA.

Preparation of C_{60}-Labeled Peptide ($PepC_{60}$). Peptide H_2N-$GSGA_3GLSH_6$ was custom synthesized using standard solid-phase peptide synthesis on Rink amide resin.[63] The unique N-terminal primary amine on the peptide was site-specifically labeled with C_{60}-pyrrolidine tris-acid (Sigma-Aldrich, St. Louis, MO) and purified using procedures similar to those described previously[64] with slight modifications. Briefly, peptide (3.7 mg, 2.45 μmol), C_{60}-pyrrolidine tris-acid (8.6 mg, 9.45 μmol), *N*-hydroxysuccinimide (23.6 mg, 205 μmol), and *N,N′*-dicyclohexylcarbodiimide (33.5 mg, 162 μmol) were added to a 20 mL scintillation vial. (Note: this coupling reaction can be performed by replacing *N,N′*-dicyclohexylcarbodiimide with *N,N′*-diisopropylcarbodiimide.) The reagents were dissolved in 3 mL of 95% DMSO/H_2O and mixed with a stir bar overnight at room temperature (~16−20 h). This reaction has a 3.9-fold excess of C_{60} to peptide, and in combination with steric hindrance, this was optimized to yield a 1:1 C_{60}:peptide coupling. To isolate $pepC_{60}$, 4 mL of Ni^{2+}-nitrilotriacetic acid (Ni-NTA) agarose resin (Qiagen) was added to the reaction mixture and the mixture was agitated on a rotary mixer for 1 h. The resin was then filtered through a filter frit and washed with a copious amount of DMSO (~45 mL) and then H_2O (~20 mL). In both wash steps, the resin was washed

until the filtrate was colorless. The $pepC_{60}$ was eluted from the resin using 3−4 mL of a 300 mM imidazole (aq)/DMSO (50/50) solution. The resulting filtrate was desalted on a preprimed oligonucleotide purification cartridge (OPC) and dried to a pellet.[64] The $pepC_{60}$ pellet was dissolved in DMSO, quantified by UV−vis spectrophotometry (C_{60} $\varepsilon_{\lambda 350\ nm}$ = 34 300 M^{-1} cm^{-1}), and then stored frozen at −20 °C in a desiccator.

Self Assembly of Quantum Dot−$PepC_{60}$ Conjugates. Frozen $pepC_{60}$ DMSO samples were thawed, sonicated, and used to prepare diluted stock solutions of $pepC_{60}$ in DMSO. The following is an example of how conjugates were assembled for steady-state fluorescence and excited-state lifetime analysis. First, QDs (20 pmol, 1 μM) in 13 mM sodium tetraborate buffer pH 8.5 were mixed with additional borate buffer (20 μL) and DMSO. For other experiments, phosphate buffered saline (1 × PBS, 10 mM phosphate, 137 mM NaCl, 3 mM KCl, pH 7.4) was used. Appropriate volumes of $pepC_{60}$ stock solutions in DMSO were added to the QD mixtures to achieve the desired $pepC_{60}$/QD ratios. The final assemblies were in a total volume of 115 μL, where the initial volume of additional DMSO added was adjusted to achieve ∼65% DMSO (v/v) or another desired DMSO concentration. The conjugates were analyzed after allowing mixing and assembly overnight.

Differential Pulse Voltammetry (DPV). DPV measurements were performed in a Faraday cage in the three-electrode geometry with a microvolume cell, using a glassy carbon working electrode, a Pt counter electrode, and a Ag/AgCl 3 M KCl reference electrode under Ar gas at ambient conditions. Measurements were driven by an electrochemical workstation Model 750 from CH Instruments (Austin, TX) using solutions of C_{60}-pyrrolidine tris-acid (124 μM) and $pepC_{60}$ (103 μM) in 200 μL of DMSO:0.5×PBS (3:1). Background voltammograms were collected and subtracted from the raw data.

Dynamic Light Scattering (DLS). DLS measurements were performed using a CGS-3 goniometer system equipped with a HeNe laser (633 nm) and a single-photon counting avalanche photodiode (Malvern Instruments, Southborough, MA). Autocorrelation functions were performed by an ALV-5000/EPP photon correlator (ALV, Langen, Germany) and analyzed with Dispersion Technology Software (DTS, Malvern Instruments). The neat QD solutions in 65% DMSO/water were filtered through 0.2 μm syringe filters (Millipore Corporation) prior to DLS measurements. QD solutions self-assembled with $pepC_{60}$ in 65% DMSO/water were filtered through 0.45 μm syringe filters (Millipore Corporation). The sample temperature was maintained at 20 °C. For each sample, the autocorrelation function was the average of three runs of 10 s each and then repeated at different scattering angles (within 70° and 120°). CONTIN analysis was then used to extract number versus hydrodynamic size profiles for the dispersions studied similar to that described previously.[65]

Optical Characterization. Electronic absorption spectra were collected on an HP 8453 diode array spectrophotometer (Agilent Technologies, Santa Clara, CA, USA). Fluorescence spectra were recorded on either a Spex Fluorolog-3 spectrophotometer (Jobin Yvon Inc., Edison, NJ, USA) equipped with a 450 nm CVI long wave pass filter or a Tecan Infinite M1000 fluorescence multifunction plate reader.

Excited-State Fluorescent Lifetime Analysis. Excited-state lifetime measurements were made using 375 and 471 nm Becker & Hickl diode laser excitation sources with 50 ps pulse widths operating at 20 MHz. Fluorescence signals were detected with a Hamamatsu 8309U-50 MCP-PMT and processed with a Becker & Hickl time-correlated single photon counting system. Prior to analysis, the decays were background corrected and the data were fit with biexponential decay functions using PicoQuant fitting routines.

Transient Absorption Analysis. Optical femtosecond transient absorption (fsTA) measurements were performed with an apparatus based on a commercial amplified Ti:sapphire laser system (Spectra-Physics Mira Oscillator and Spitfire Pro Amplifier) at 1.7 kHz and carried out at either the Center for Nanoscale Materials at Argonne National Laboratory or the Center for Functional Nanomaterials at Brookhaven National Laboratory. A small amount of the amplifier output was used to generate the white light continuum probe, and the remaining 95% went through an optical parametric amplifier (OPA) to produce 420 nm excitation pulses at 0.7 μJ/pulse. The data were collected through a Helios spectrometer (Ultrafast Systems), where the probe is delayed relative to the pump on a mechanical delay line. The pump beam is chopped at half the repetition rate of the laser, so that the absorption change (ΔA) can be measured as a function of delay time, where $\Delta A = -\log(I_{pump+probe}/I_{probe})$. The data were chirp-corrected using a solvent blank to within 100 fs over the spectral range of 440−770 nm used here. The samples were placed in a 2 mm quartz cuvette and stirred during the acquisition. The widths of the pump and probe pulses were estimated at about 120 fs. The transient absorption changes for a particular probe wavelength as a function of time were analyzed by fitting the kinetics with a multiexponential model convoluted with a Gaussian instrument response function displaying a 200 fs full width at half-maximum (fwhm). Samples for fsTA were freshly prepared each day, and the data are an average of three spectra. The fsTA of 580-nm-emitting QDs in 1×PBS was performed using photoexcitation at 420 nm in solutions with concentrations ranging from 0.1 to 0.5 μM. Freshly mixed solutions of QDs and $pepC_{60}$ using an assembly ratio of 20:1 (10 μM $pepC_{60}$:0.5 μM 580 nm QD) and 80:1 (10 μM $pepC_{60}$:0.1 μM 580 nm QD) $pepC_{60}$:QD, and control samples of only $pepC_{60}$ or QDs, were prepared in PBS using stock solutions for each experiment.

Förster Resonance Energy Transfer Analysis. The overlap integral J between the QD PL spectra and $pepC_{60}$ absorption spectrum in units of cm^3 M^{-1} was calculated using:[66]

$$J = \int_0^\infty J(\lambda)\, d\lambda \tag{1}$$

where $J(\lambda)$, the spectral overlap, is integrated over the portion of the spectrum where the QD is emissive and is given by the expression:

$$J(\lambda) = F_D(\lambda)\, \varepsilon_A(\lambda)\, \lambda^4 \tag{2}$$

$F_D(\lambda)$ is the dimensionless normalized fluorescence intensity of the donor QD at λ; ε_A is the extinction coefficient of the acceptor at λ (M^{-1} cm^{-1}); and λ is the wavelength (cm). The Förster distance R_0 in units of Å corresponding to 50% energy transfer efficiency between the donor and acceptor pair was determined by:[65]

$$R_0 = 9.78 \times 10^3 [\kappa^2 n^{-4} Q_D J]^{1/6} \tag{3}$$

where a dipole orientation factor of $\kappa^2 = 2/3$ was used as shown to be appropriate for such randomly assembled QD conjugates,[67] n is the refractive index of the medium, Q_D is the quantum yield of the donor, and J is as defined above. We used a refractive index value of 1.38 based on the refractive index values published for DMSO−water mixtures.[68] The estimated FRET efficiency was obtained using the expression:

$$\eta_{FRET} = N \Big/ \left\{ N + \left(\frac{r}{R_0} \right)^6 \right\} \tag{4}$$

where N is the number of acceptors appended to the QD, and r is the average center-to-center distance between the QD and the C_{60} which was estimated as described below. Thus, the greater the spectral overlap between the QD emission and the C_{60} absorption, the larger the values of R_0 and FRET efficiency, η_{FRET}. The estimated FRET efficiency can also be defined using the expression:

$$\eta_{FRET} = N k_{FRET} / k_{Total} \tag{5}$$

where k_{Total} is the total decay rate and is equal to the inverse of the measured luminescence lifetime of the QD in the C_{60} complex. The FRET rate constants can then be determined by combining eqs 4 and 5.

Wavelength Dependent FRET Analysis. A unique characteristic of FRET between a QD donor and a broad band acceptor is that the quenching efficiency displays a wavelength dependence across the QD PL band that results in a distortion of the shape and/or the position of the peak of the quenched PL relative to the unquenched band. Although the shifts are relatively small, and

are typically not taken into account for most QD-FRET-based measurements, they are significant in the sense that they can be used to differentiate between FRET and other quenching mechanisms that are not strongly wavelength dependent on the underlying spectral overlap. We modeled the QD PL emission spectra using a series of Gaussian line-shape functions with spectral widths of ~15 nm and calculated the spectral overlap integrals using eqs 1 and 2 for each contributor to the overall PL spectrum, where J depends on the value of the acceptor extinction coefficient at the peak wavelength of each component. Values for R_0 and the expected FRET efficiency for each component were calculated using eqs 3 and 4. This allowed us to extract the wavelength dependent FRET quenching efficiency in a manner similar to that described in detail in refs 38, 52, and 53.

Energy Transfer Kinetic Analysis. For the purposes of our analysis, we assume that PL quenching in the QD−pepC_{60} complexes is limited to contributions from ET and FRET. It is not possible to determine the magnitudes of these contributions directly from our steady state and lifetime quenching studies, but we can estimate the theoretical FRET efficiencies based on the overlap integral and the corresponding values determined for R_0. The total quenching efficiency, η_Q, can then be obtained from the following expressions:

$$\eta_Q = \left(1 - \frac{I_N}{I_0}\right) = \left(1 - \frac{\tau_N}{\tau_0}\right) \quad (6)$$

where I_N is the fluorescence intensity of the QD complex with N appended acceptors, I_0 is the fluorescence intensity of the QDs without acceptors, τ_N is the luminescence lifetime of the QD complex with N acceptors, and τ_0 is the QD lifetime in the absence of acceptors. The total decay rate (k_{Total}) of the QD−(pepC_{60})$_N$ complex is equal to the sum of all of the potential deactivation rates:

$$k_{Total} = k_r + k_{nr} + Nk_{FRET} + Nk_{ET} = \frac{1}{\tau_N} \quad (7)$$

where τ_N is the luminescence lifetime of the complex measured on the nanosecond time scale, k_r is the radiative decay rate, k_{nr} is the nonradiative decay rate, k_{ET} is the ET rate, and k_{FRET} is the FRET rate. Following with this:

$$k_r + k_{nr} = k_0 = \frac{1}{\tau_0} \quad (8)$$

where k_0 is the decay rate of the QD itself in the absence of C_{60}. The series of experiments in which the number of pepC_{60} units per QD was varied thus provides a handle for estimating the FRET efficiency as well as the FRET rate. The ET rate, k_{ET}, was estimated from the expression:

$$Nk_{ET} = k_{total} - Nk_{FRET} - k_0 \quad (9)$$

and the ET efficiency was estimated from the expression:

$$\eta_{ET} = Nk_{ET}/k_{Total} \quad (10)$$

Structural Simulations. All models were created using tools in UCSF Chimera, version 1.4.1.[69] Energy minimization was carried out in Chimera using built-in features including ANTECHAMBER (version 1.27) and the AM1-BCC method of calculating charges.[70] The model of the C_{60} was constructed from the structure of (η^5-pentaphenyl-C_{60}fullerene)-(η^5-cyclopentadienyl)-iron carbon disulfide.[71] The covalently attached phenyl groups were removed from the C_{60} using the tools in Chimera, and the resulting model was energy minimized as described above. The C_{60} was further modified to contain the same bridging group as used in the constructs on the region formerly occupied by the phenyl groups. A peptide linker with the sequence GSGAAAGLSHHHHHH was created in Chimera. Based on prior work, the His_6 region was modeled with an extended conformation, which is consistent with the 4−6 coordination bonds the His_6 tail forms with the QD surface.[39] The SGAAA region was modeled as a helix based on both energy minimization and structural similarity to other short peptides of known conformation. After allowing these constraints, the model was again energy minimized at this stage. The models for the C_{60} and peptide linker were joined, and the full model was then also energy minimized. This model was docked to the surface of the QD approximated by a sphere with a radius of 30 Å. In the partially folded conformation shown in Figure 5B, the distance from the QD center to the center of the C_{60} is 55.5 Å. A fully extended peptide (not shown) would result in a QD−C_{60} separation of 63.4 Å, and a tightly folded conformation (not shown) would result in the C_{60} in direct contact with the QD surface. The latter, tightly folded conformation is unlikely energetically due to the presence of steric hindrance by the DHLA ligands on the QD surface and charge repulsion along with necessitating the peptide to assume an unfavored, higher-energy conformation.

Conflict of Interest: The authors declare no competing financial interest.

Acknowledgment. The authors acknowledge NRL NSI and DTRA JSTO MIPR # B112582M for financial support. The authors thank S. Trammell for assistance with collecting DPV data. Molecular graphics images were produced using the UCSF Chimera package from the Resource for Biocomputing, Visualization, and Informatics at the University of California, San Francisco (supported by NIH P41 RR-01081).

Supporting Information Available: Includes control experiments, TEM data, selected methods and other supporting results. This material is available free of charge *via* the Internet at http://pubs.acs.org.

REFERENCES AND NOTES

1. Ip, A. H.; Thon, S. M.; Hoogland, S.; Voznyy, O.; Zhitomirsky, D.; Debnath, R.; Levina, L.; Rollny, L. R.; Carey, G. H.; Fischer, A.; et al. Hybrid Passivated Colloidal Quantum Dot Solids. *Nat. Nanotechnol.* **2012**, *7*, 577–582.
2. Geyer, S. M.; Scherer, J. M.; Moloto, N.; Jaworski, F. B.; Bawendi, M. G. Efficient Luminescent Down-Shifting Detectors Based on Colloidal Quantum Dots for Dual-Band Detection Applications. *ACS Nano* **2011**, *5*, 5566–5571.
3. Sukhovatkin, V.; Hinds, S.; Brzozowski, L.; Sargent, E. H. Colloidal Quantum-Dot Photodetectors Exploiting Multiexciton Generation. *Science* **2009**, *324*, 1542–1544.
4. Sun, L. F.; Choi, J. J.; Stachnik, D.; Bartnik, A. C.; Hyun, B. R.; Malliaras, G. G.; Hanrath, T.; Wise, F. W. Bright Infrared Quantum-Dot Light-Emitting Diodes Through Inter-Dot Spacing Control. *Nat. Nanotechnol.* **2012**, *7*, 369–373.
5. Qian, L.; Zheng, Y.; Xue, J. G.; Holloway, P. H. Stable and Efficient Quantum-Dot Light-Emitting Diodes Based on Solution-Processed Multilayer Structures. *Nat. Photonics* **2011**, *5*, 543–548.
6. Petryayeva, E.; Medintz, I. L.; Algar, W. R. Quantum Dots in Bioanalysis: A Review of Applications Across Various Platforms for Fluorescence Spectroscopy and Imaging. *Appl. Spectrosc.* **2013**, *67*, 215–252.
7. Algar, W. R.; Susumu, K.; Delehanty, J. B.; Medintz, I. L. Quantum Dots in Bioanalysis: Crossing the Valley of Death. *Anal. Chem.* **2011**, *83*, 8826–8837.
8. Rosenthal, S. J.; Chang, J. C.; Kovtun, O.; McBride, J. R.; Tomlinson, I. D. Biocompatible Quantum Dots for Biological Applications. *Chem. Biol.* **2011**, *18*, 10–24.
9. Shirasaki, Y.; Supran, G. J.; Bawendi, M. G.; Bulovic, V. Emergence of Colloidal Quantum-Dot Light-Emitting Technologies. *Nat. Photonics* **2013**, *7*, 13–23.
10. Algar, W. R.; Tavares, A. J.; Krull, U. J. Beyond Labels: A Review of the Application of Quantum Dots as Integrated Components of Assays, Bioprobes, and Biosensors Utilizing Optical Transduction. *Anal. Chim. Acta* **2010**, *673*, 1–25.
11. Raymo, F. M.; Yildiz, I. Luminescent Chemosensors Based on Semiconductor Quantum Dots. *Phys. Chem. Chem. Phys.* **2007**, *9*, 2036–2043.
12. Algar, W. R.; Malonoski, A.; Deschamps, J. R.; Banco-Canosa, J. B.; Susumu, K.; Stewart, M. H.; Johnson, B. J.; Dawson, P. E.; Medintz, I. L. Proteolytic Activity at Quantum Dot-Conjugates: Kinetic Analysis Reveals Enhanced Enzyme Activity and Localized Interfacial "Hopping". *Nano Lett.* **2012**, *12*, 3793–3802.

13. Bang, J. H.; Kamat, P. V. CdSe Quantum Dot-Fullerene Hybrid Nanocomposite for Solar Energy Conversion: Electron Transfer and Photoelectrochemistry. *ACS Nano* **2011**, *5*, 9421–9427.
14. Song, N. H.; Zhu, H. M.; Jin, S. Y.; Zhan, W.; Lian, T. Q. Poisson-Distributed Electron-Transfer Dynamics from Single Quantum Dots to C60 Molecules. *ACS Nano* **2011**, *5*, 613–621.
15. Gocalinska, A.; Saba, M.; Quochi, F.; Marceddu, M.; Szendrei, K.; Gao, J.; Loi, M. A.; Yarema, M.; Seyrkammer, R.; Heiss, W.; *et al.* Size-Dependent Electron Transfer from Colloidal PbS Nanocrystals to Fullerene. *J. Phys. Chem. Lett.* **2010**, *1*, 1149–1154.
16. Xu, Z. H.; Cotlet, M. Quantum Dot-Bridge-Fullerene Heterodimers with Controlled Photoinduced Electron Transfer. *Angew. Chem., Int. Ed.* **2011**, *50*, 6079–6083.
17. Schulz-Drost, C.; Sgobba, V.; Gerhards, C.; Leubner, S.; Calderon, R. M. K.; Ruland, A.; Guldi, D. M. Innovative Inorganic-Organic Nanohybrid Materials: Coupling Quantum Dots to Carbon Nanotubes. *Angew. Chem., Int. Ed* **2010**, *49*, 6425–6429.
18. Weaver, J. E.; Dasari, M. R.; Datar, A.; Talapatra, S.; Kohli, P. Investigating Photoinduced Charge Transfer in Carbon Nanotube-Perylene-Quantum Dot Hybrid Nanocomposites. *ACS Nano* **2010**, *4*, 6883–6893.
19. Lu, F. S.; Haque, S. A.; Yang, S. T.; Luo, P. G.; Gu, L. R.; Kitaygorodskiy, A.; Li, H. P.; Lacher, S.; Sun, Y. P. Aqueous Compatible Fullerene-Doxorubicin Conjugates. *J. Phys. Chem. C* **2009**, *113*, 17768–17773.
20. Katsukis, G.; Romero-Nieto, C.; Malig, J.; Ehli, C.; Guldi, D. M. Interfacing Nanocarbons with Organic and Inorganic Semiconductors: From Nanocrystals/Quantum Dots to Extended Tetrathiafulvalenes. *Langmuir* **2012**, *28*, 11662–11675.
21. Shibu, E. S.; Sonoda, A.; Tao, Z. Q.; Feng, Q.; Furube, A.; Masuo, S.; Wang, L.; Tamai, N.; Ishikawa, M.; Biju, V. Photofabrication of Fullerene-Shelled Quantum Dots Supramolecular Nanoparticles for Solar Energy Harvesting. *ACS Nano* **2012**, *6*, 1601–1608.
22. Guldi, D. M.; Zilbermann, I.; Anderson, G.; Kotov, N. A.; Tagmatarchis, N.; Prato, M. Versatile Organic (Fullerene) - Inorganic (CdTe Nanoparticle) Nanoensembles. *J. Am. Chem. Soc.* **2004**, *126*, 14340–14341.
23. Nandwana, V.; Serrano, L. A.; Solntsev, K. M.; Ebenhoch, B.; Liu, Q.; Tonga, G. Y.; Samuel, I. D.; Cooke, G.; Rotello, V. M. Engineering the Nanoscale Morphology of a Quantum Dot-Fullerene Assembly *via* Complementary Hydrogen Bonding Interactions. *Langmuir* **2013**, *29*, 7534–7537.
24. Liu, D. F.; Wu, W.; Qiu, Y. F.; Lu, J.; Yang, S. H. Chemical Conjugation of Fullerene C-60 to CdSe Nanocrystals *via* Dithiocarbamate Ligands. *J. Phys. Chem. C* **2007**, *111*, 17713–17719.
25. Szendrei, K.; Jarzab, D.; Yarema, M.; Sytnyk, M.; Pichler, S.; Hummelen, J. C.; Heiss, W.; Loi, M. A. Surface Modification of Semiconductor Nanocrystals by a Methanofullerene Carboxylic Acid. *J. Mater. Chem.* **2010**, *20*, 8470–8473.
26. Lightcap, I. V.; Kamat, P. V. Fortification of CdSe Quantum Dots with Graphene Oxide. Excited State Interactions and Light Energy Conversion. *J. Am. Chem. Soc.* **2012**, *134*, 7109–7116.
27. Peng, X. H.; Misewich, J. A.; Wong, S. S.; Sfeir, M. Y. Efficient Charge Separation in Multidimensional Nanohybrids. *Nano Lett.* **2011**, *11*, 4562–4568.
28. Chen, Z. Y.; Berciaud, S.; Nuckolls, C.; Heinz, T. F.; Brus, L. E. Energy Transfer from Individual Semiconductor Nanocrystals to Graphene. *ACS Nano* **2010**, *4*, 2964–2968.
29. Shafran, E.; Mangum, B. D.; Gerton, J. M. Energy Transfer from an Individual Quantum Dot to a Carbon Nanotube. *Nano Lett.* **2010**, *10*, 4049–4054.
30. Biju, V.; Itoh, T.; Baba, Y.; Ishikawa, M. Quenching of Photoluminescence in Conjugates of Quantum Dots and Single-Walled Carbon Nanotube. *J. Phys. Chem. B* **2006**, *110*, 26068–26074.
31. Morales-Narvaez, E.; Perez-Lopez, B.; Pires, L. B.; Merkoc, A. Simple Forster Resonance Energy Transfer Evidence for the Ultrahigh Quantum Dot Quenching Efficiency by Graphene Oxide Compared to Other Carbon Structures. *Carbon* **2012**, *50*, 2987–2993.
32. Li, M.; Zhou, X.; Guo, S.; Wu, M. Detection of Lead(II) with a "Turn-On" Fluorescent Biosensor Based on Energy Transfer from CdSe/ZnS Quantum Dots to Graphene Oxide. *Biosens. Bioelectron.* **2013**, *42*, 69–74.
33. Boeneman, K.; Delehanty, J. B.; Susumu, K.; Stewart, M. H.; Medintz, I. L. Intracellular Bioconjugation of Targeted Proteins with Semiconductor Quantum Dots. *J. Am. Chem. Soc.* **2010**, *132*, 5975–5977.
34. Delehanty, J. B.; Bradburne, C. E.; Boeneman, K.; Susumu, K.; Farrell, D.; Mei, B. C.; Blanco-Canosa, J. B.; Dawson, G.; Dawson, P. E.; Mattoussi, H.; *et al.* Delivering Quantum Dot-Peptide Bioconjugates to the Cellular Cytosol: Escaping from the Endolysosomal System. *Integr. Biol.* **2010**, *2*, 265–277.
35. Prasuhn, D. E.; Feltz, A.; Blanco-Canosa, J. B.; Susumu, K.; Stewart, M. H.; Mei, B. C.; Yakovlev, A. V.; Loukov, C.; Mallet, J. M.; Oheim, M.; *et al.* Quantum Dot Peptide Biosensors for Monitoring Caspase 3 Proteolysis and Calcium Ions. *ACS Nano* **2010**, *4*, 5487–5497.
36. Sapsford, K. E.; Algar, W. R.; Berti, L.; Gemmill, K. B.; Casey, B. J.; Oh, E.; Stewart, M. H.; Medintz, I. L. Functionalizing Nanoparticles with Biological Molecules: Developing Chemistries that Facilitate Nanotechnology. *Chem. Rev.* **2013**, *113*, 1904–2074.
37. Peng, X. G.; Schlamp, M. C.; Kadavanich, A. V.; Alivisatos, A. P. Epitaxial Growth of Highly Luminescent CdSe/CdS Core/Shell Nanocrystals with Photostability and Electronic Accessibility. *J. Am. Chem. Soc.* **1997**, *119*, 7019–7029.
38. Stewart, M. H.; Huston, A. L.; Scott, A. M.; Efros, A. L.; Melinger, J. S.; Gemmill, K. B.; Trammell, S. A.; Blanco-Canosa, J. B.; Dawson, P. E.; Medintz, I. L. Complex Forster Energy Transfer Interactions between Semiconductor Quantum Dots and a Redox-Active Osmium Assembly. *ACS Nano* **2012**, *6*, 5330–5347.
39. Sapsford, K. E.; Pons, T.; Medintz, I. L.; Higashiya, S.; Brunel, F. M.; Dawson, P. E.; Mattoussi, H. Kinetics of Metal-Affinity Driven Self-Assembly Between Proteins or Peptides and CdSe-ZnS Quantum Dots. *J. Phys. Chem. C* **2007**, *111*, 11528–11538.
40. Algar, W. R.; Prasuhn, D. E.; Stewart, M. H.; Jennings, T. L.; Blanco-Canosa, J. B.; Dawson, P. E.; Medintz, I. L. The Controlled Display of Biomolecules on Nanoparticles: A Challenge Suited to Bioorthogonal Chemistry. *Bioconjug. Chem.* **2011**, *22*, 825–858.
41. Prasuhn, D. E.; Deschamps, J. R.; Susumu, K.; Stewart, M. H.; Boeneman, K.; Blanco-Canosa, J. B.; Dawson, P. E.; Medintz, I. L. Polyvalent Display and Packing of Peptides and Proteins on Semiconductor Quantum Dots: Predicted *versus* Experimental Results. *Small* **2010**, *6*, 555–564.
42. Huang, J.; Huang, Z. Q.; Yang, Y.; Zhu, H. M.; Lian, T. Q. Multiple Exciton Dissociation in CdSe Quantum Dots by Ultrafast Electron Transfer to Adsorbed Methylene Blue. *J. Am. Chem. Soc.* **2010**, *132*, 4858–4864.
43. Knowles, K. E.; Tice, D. B.; McArthur, E. A.; Solomon, G. C.; Weiss, E. A. Chemical Control of the Photoluminescence of CdSe Quantum Dot-Organic Complexes with a Series of Para-Substituted Aniline Ligands. *J. Am. Chem. Soc.* **2010**, *132*, 1041–1050.
44. Burda, C.; Green, T. C.; Link, S.; El-Sayed, M. A. Electron Shuttling Across the Interface of CdSe Nanoparticles Monitored by Femtosecond Laser Spectroscopy. *J. Phys. Chem. B* **1999**, *103*, 1783–1788.
45. Araki, Y.; Yasumura, Y.; Ito, O. Photoinduced Electron Transfer Competitive with Energy Transfer of the Excited Triplet State of [60]Fullerene to Ferrocene Derivatives Revealed by Combination of Transient Absorption and Thermal Lens Measurements. *J. Phys. Chem B* **2005**, *109*, 9843–9848.
46. Subramanian, V.; Wolf, E. E.; Kamat, P. V. Catalysis with TiO_2/Gold Nanocomposites. Effect of Metal Particle Size on the Fermi Level Equilibration. *J. Am. Chem. Soc.* **2004**, *126*, 4943–4950.

47. Baumgarten, M.; Gugel, A.; Gherghel, L. EPR and Optical-Absorption Spectra of Reduced Buckminsterfullerene. *Adv. Mater.* **1993**, *5*, 458–461.
48. Dimitrijevic, N. M.; Kamat, P. V. Excited-State Behavior and One-Electron Reduction of C60 in Aqueous Gamma-Cyclodextrin Solution. *J. Phys. Chem. C* **1993**, *97*, 7623–7626.
49. Kucur, E.; Riegler, J.; Urban, G. A.; Nann, T. Determination of Quantum Confinement in CdSe Nanocrystals by Cyclic Voltammetry. *J. Chem. Phys.* **2003**, *119*, 2333–2337.
50. Impellizzeri, S.; Monaco, S.; Yildiz, I.; Amelia, M.; Credi, A.; Raymo, F. M. Structural Implications on the Electrochemical and Spectroscopic Signature of CdSe-ZnS Core-Shell Quantum Dots. *J. Phys. Chem C* **2010**, *114*, 7007–7013.
51. Medintz, I. L.; Mattoussi, H. Quantum Dot-Based Resonance Energy Transfer and its Growing Application in Biology. *Phys. Chem. Chem. Phys.* **2009**, *11*, 17–45.
52. Pons, T.; Medintz, I. L.; Sykora, M.; Mattoussi, H. Spectrally Resolved Energy Transfer Using Quantum Dot Donors: Ensemble and Single-Molecule Photoluminescence Studies. *Phys. Rev. B* **2006**, *73*, 245302.
53. Pons, T.; Medintz, I. L.; Sapsford, K. E.; Higashiya, S.; Grimes, A. F.; English, D. S.; Mattoussi, H. On the Quenching of Semiconductor Quantum Dot Photoluminescence by Proximal Gold Nanoparticles. *Nano Lett.* **2007**, *7*, 3157–3164.
54. Gray, H. B.; Winkler, J. R. Electron Tunneling Through Proteins. *Q. Rev. Biophys.* **2003**, *36*, 341–372.
55. Cordes, M.; Giese, B. Electron Transfer in Peptides and Proteins. *Chem. Soc. Rev.* **2009**, *38*, 892–901.
56. Albero, J.; Riente, P.; Clifford, J. N.; Pericàs, M. A.; Palomares, E. J. Improving CdSe Quantum Dot/Polymer Solar Cells Efficiency Through the Covalent Functionalization of Quantum Dots:Implications in the Devices Recombination Kinetics. *J. Phys. Chem. C* **2013**, *117*, 13374–13381.
57. Mei, B. C.; Susumu, K.; Medintz, I. L.; Mattoussi, H. Polyethylene Glycol-Based Bidentate Ligands to Enhance Quantum Dot and Gold Nanoparticle Stability in Biological Media. *Nat. Protoc.* **2009**, *4*, 412–423.
58. Susumu, K.; Oh, E.; Delehanty, J. B.; Blanco-Canosa, J. B.; Johnson, B. J.; Jain, V.; Hervey, W. J.; Algar, W. R.; Boeneman, K.; Dawson, P. E.; et al. Multifunctional Compact Zwitterionic Ligands for Preparing Robust Biocompatible Semiconductor Quantum Dots and Gold Nanoparticles. *J. Am. Chem. Soc.* **2011**, *133*, 9480–9496.
59. Li, J. J.; Wang, Y. A.; Guo, W. Z.; Keay, J. C.; Mishima, T. D.; Johnson, M. B.; Peng, X. G. Large-Scale Synthesis of Nearly Monodisperse CdSe/CdS Core/Shell Nanocrystals Using Air-Stable Reagents *via* Successive Ion Layer Adsorption and Reaction. *J. Am. Chem. Soc.* **2003**, *125*, 12567–12575.
60. Blackman, B.; Battaglia, D.; Peng, X. G. Bright and Water-Soluble Near IR-Emitting CdSe/CdTe/ZnSe Type-II/Type-I Nanocrystals, Tuning the Efficiency and Stability by Growth. *Chem. Mater.* **2008**, *20*, 4847–4853.
61. Blackman, B.; Battaglia, D. M.; Mishima, T. D.; Johnson, M. B.; Peng, X. G. Control of the Morphology of Complex Semiconductor Nanocrystals with a Type II Heterojunction, Dots *vs* Peanuts, by Thermal Cycling. *Chem. Mater.* **2007**, *19*, 3815–3821.
62. Liu, D.; Snee, P. T. Water-Soluble Semiconductor Nanocrystals Cap Exchanged with Metalated Ligands. *ACS Nano* **2011**, *5*, 546–550.
63. Schnolzer, M.; Alewood, P.; Jones, A.; Alewood, D.; Kent, S. B. H. *In situ* Neutralization in BOC-Chemistry Solid-Phase Peptide-Synthesis. Rapid, High-Yield Assembly of Difficult Sequences. *Int. J. Pep. Prot. Res.* **1992**, *40*, 180–193.
64. Sapsford, K. E.; Farrell, D.; Sun, S.; Rasooly, A.; Mattoussi, H.; Medintz, I. L. Monitoring of Enzymatic Proteolysis on a Electroluminescent-CCD Microchip Platform using Quantum Dot-Peptide Substrates. *Sens. Actuators B, Chem.* **2009**, *139*, 13–21.
65. Oh, E.; Fatemi, F.; Currie, M.; Delehanty, J. B.; Pons, T.; Fragola, A.; Lévêque-Fort, S.; Goswami, R.; Susumu, K.; Huston, A.; *et al.* PEGylated Luminescent Gold Nanoclusters: Synthesis, Characterization, Bioconjugation and Application to One- and Two-Photon Cellular Imaging. *Part. Part. Syst. Charact.* **2013**, *30*, 453–466.
66. Lakowicz, J. R. *Principles of Fluorescence Spectroscopy*, 2nd ed.; Kluwer Academic/Plenum: New York, 1999.
67. Clapp, A. R.; Medintz, I. L.; Mauro, J. M.; Fisher, B. R.; Bawendi, M. G.; Mattoussi, H. Fluorescence Resonance Energy Transfer Between Quantum Dot Donors and Dye-Labeled Protein Acceptors. *J. Am. Chem. Soc.* **2004**, *126*, 301–310.
68. LeBel, R. G.; CGoring, D. A. I. Density, Viscosity, Refractive Index, and Hygroscopicity of Mixtures of Water and Dimethyl Sulfoxide. *J. Chem. Eng. Data* **1962**, *7*, 100–101.
69. Pettersen, E. F.; Goddard, T. D.; Huang, C. C.; Couch, G. S.; Greenblatt, D. M.; Meng, E. C.; Ferrin, T. E. UCSF Chimera - A Visualization System for Exploratory Research and Analysis. *J. Comput. Chem.* **2004**, *25*, 1605–1612.
70. Wang, J.; Wang, W.; Kollman, P. A.; Case, D. A. Automatic Atom Type and Bond Type Perception in Molecular Mechanical Calculations. *J. Mol. Graph. Model.* **2006**, *25*, 247–260.
71. Herber, R. H.; Nowik, I.; Matsuo, Y.; Toganoh, M.; Kuninobu, Y.; Nakamura, E. Mossbauer Spectroscopy of Bucky Ferrocenes: Lattice Dynamics and Motional Anisotropy of the Metal Atom. *Inorg. Chem.* **2005**, *44*, 5629–5635.